

**Constraining Black Carbon Aerosol over Asia using  
OMI Aerosol Absorption Optical Depth and the  
Adjoint of GEOS-Chem**

**Li Zhang<sup>1,2</sup>, Daven K. Henze<sup>1</sup>, Georg A. Grell<sup>2</sup>, Gregory R. Carmichael<sup>3</sup>, Nicolas  
Bousserez<sup>1</sup>, Qiang Zhang<sup>4</sup>, Omar Torres<sup>5</sup>, Changwoo Ahn<sup>6</sup>, Zifeng Lu<sup>7</sup>, Junji  
Cao<sup>8</sup>, Yuhao Mao<sup>9, 10</sup>**

<sup>1</sup>Department of Mechanical Engineering, University of Colorado, Boulder, CO, USA

<sup>2</sup>Global Systems Division, Earth System Research Laboratory, NOAA, Boulder, CO,  
USA

<sup>3</sup>Department of Chemical and Biochemical Engineering, University of Iowa, Iowa, IA,  
USA

<sup>4</sup>Center for Earth System Science, Tsinghua University, Beijing, China

<sup>5</sup>NASA Goddard Space Flight Center, Greenbelt, MD, USA

<sup>6</sup>Science Systems and Applications, Inc., Lanham, MD, USA

<sup>7</sup>Decision and Information Sciences Division, Argonne National Laboratory, Argonne,  
IL, USA

<sup>8</sup>Key Lab of Aerosol Chemistry & Physics, Institute of Earth Environment, Chinese  
Academy of Sciences, Xi'an, China

<sup>9</sup>Department of Atmospheric and Oceanic Sciences, University of California, Los  
Angeles, CA, USA

<sup>10</sup>State Key Laboratory of Atmospheric Boundary Layer Physics and Atmospheric  
Chemistry, Institute of Atmospheric Physics, Chinese Academy of Sciences, Beijing,  
China

Submitted to Atmospheric Chemistry and Physics

September 2015

\*Corresponding author:  
daven.henze@colorado.edu  
Dept. of Mechanical Engineering  
1111 Engineering Drive ECES 114  
University of Colorado, Boulder  
Boulder, CO 80309

1   **Abstract**

2   Accurate estimates of the emissions and distribution of black carbon (BC) in the  
3   region referred to here as Southeastern Asia (70°E–150°E, 11°S–55°N) are critical to  
4   studies of the atmospheric environment and climate change. Analysis of modeled BC  
5   concentrations compared to in situ observations indicates levels are underestimated  
6   over most of Southeast Asia when using any of four different emission inventories.  
7   We thus attempt to reduce uncertainties in BC emissions and improve BC model  
8   simulations by developing top-down, spatially resolved, estimates of BC emissions  
9   through assimilation of OMI observations of aerosol absorption optical depth  
10   (AAOD) with the GEOS-Chem model and its adjoint for April and October of 2006.  
11   Overwhelming enhancements, up to 500%, in anthropogenic BC emissions are shown  
12   after optimization over broad areas of Southeast Asia in April. In October, the  
13   optimization of anthropogenic emissions yields a slight reduction (1~5%) over India  
14   and parts of southern China, while emissions increase by 10~50% over eastern China.  
15   Observational data from in situ measurements and AERONET observations are used  
16   to evaluate the BC inversions and assess the bias between OMI and AERONET  
17   AAOD. Low biases in BC concentrations are improved or corrected in most eastern  
18   and central sites over China after optimization, while the constrained model still  
19   underestimates concentrations in Indian sites in both April and October, possibly as a  
20   consequence of low prior emissions. Model resolution errors may contribute up to a  
21   factor of 2.5 to the underestimate of surface BC concentrations over northern India.  
22   We also compare the optimized results using different anthropogenic emission  
23   inventories and discuss the sensitivity of top-down constraints on anthropogenic  
24   emissions with respect to biomass burning emissions. In addition, the impacts of  
25   brown carbon, the formulation of the observation operator, and different a priori  
26   constraints on the optimization are investigated. Overall, despite these limitations and  
27   uncertainties, using OMI AAOD to constrain BC sources improves model  
28   representation of BC distributions, particularly over China.

29

## 1. Introduction

Black carbon (BC) is a product of incomplete combustion of carbonaceous fuels, enhanced concentrations of which have led to a present-day overall positive radiative forcing and climate warming [Charlson and Pilat, 1969; Satheesh and Ramanathan, 2000; Bond et al., 2013]. More than ten years ago, Jacobson [2000] and Hansen et al. [2000] recognized that preindustrial to present increases in BC might warm the atmosphere about one third as much as CO<sub>2</sub>. Recently, an assessment by Bond et al. [2013] indicates that the global average preindustrial to present radiative forcing from BC is +1.1 W/m<sup>2</sup> with 90% uncertainty bounds of +0.17 to +2.1 W/m<sup>2</sup>, which is more than two thirds that of CO<sub>2</sub> (+1.56 W/m<sup>2</sup>). Additionally, BC aerosols constitute up to 10-15% of the mass concentration of fine particulate matter (PM<sub>2.5</sub>) over continental regions, exposure to which is known to adversely effect human health [e.g., Janssen et al., 2005; Schwartz et al., 2008; Janssen et al., 2011]. Given the magnitude of BC climate effects and health impacts, a number of studies have investigated its direct effect [Forster 2007; Ramanathan and Carmichael, 2008], semi-direct effect [Ackerman et al., 2000; Johnson et al., 2004], indirect effect [Cozic et al., 2007; Liu et al., 2009; Oshima et al., 2009], and the albedo effect when deposited on snow [Hansen and Nazarenko, 2004; Hansen et al., 2005; Flanner et al., 2007; Qian et al., 2009] using various numerical models and observations.

Central estimates of global annual emissions of BC are 8.0 Tg, of which 38% comes from fossil fuel, 20% from biofuel and 42% from open burning [Bond et al., 2004]. At the same time, estimates of BC emissions are recognized as having large uncertainties -- 50% at global scales and a factor of two to five at regional scales

1 [Bond et al., 2004; Ramanathan and Carmichael, 2008]. The Asian region referred to  
2 here as Southeast Asia (70°E–150°E, 11°S–55°N) is the major anthropogenic BC  
3 source region in the world, with growth in BC emissions of 21% over China and 41%  
4 over India from 1996 to 2010 associated with rapid economic and industrial  
5 development [Lu et al., 2011]. BC emissions from both energy-related combustion  
6 and biomass burning that occur largely in Asia and Africa currently appear  
7 underestimated [Bond et al., 2013]. A global top-down estimate of BC emission using  
8 AERONET observation by Cohen and Wang [2014] indicated that commonly used  
9 global BC emissions datasets may be underestimated by a factor of two or more.  
10 Sixteen models from the AeroCom aerosol model intercomparison study  
11 underestimated the Southeast Asian BC surface concentrations by a factor of 2~3  
12 [Koch et al., 2009]. The GEOS-Chem model also underestimated monthly BC  
13 concentrations at almost all rural sites in China, particularly in January 2006, which  
14 indicated a regional underprediction of carbonaceous aerosol sources associated with  
15 anthropogenic activities [Fu et al., 2012; Wang et al., 2013]. In addition, the global  
16 atmospheric absorption attributable to BC is too low in many global aerosol models  
17 by a factor of almost three on a global mean basis, which can be attributed to the  
18 models lacking treatment of enhanced absorption caused by mixing of BC with other  
19 constituents and the amount of BC in the atmosphere [Koch et al., 2009; Bond et al.,  
20 2013]. On the other hand, a typical fresh particle mass absorption cross section  
21 (MABS, essentially the column BC absorption divided by the load) of about 7.5 m<sup>2</sup>  
22 g<sup>-1</sup>, a value recommended by Bond and Bergstrom [2006], is not represented in most

1 models [Koch et al., 2009]. This bias would also impact simulated AAOD, and  
2 inferences about emissions based on such comparisons would likewise be biased.

3 To reduce uncertainties in BC emissions and improve poor representation of BC in  
4 model simulations, different top-down approaches have been used to constrain  
5 bottom-up BC emissions, such as the linear constraints between concentrations and  
6 emissions [Park et al., 2003; Kondo et al., 2011; Fu et al., 2012; Wang et al., 2013],  
7 inverse modeling using the decoupled direct method [Hu et al., 2009a; Hu et al.,  
8 2009b], the Kalman filter technique [Cohen and Wang 2014], and the adjoint based  
9 4D variational approach [Hakami et al., 2005]. These studies have exclusively used in  
10 situ measurements or airborne observations, which can provide accurate observations  
11 of aerosol properties. However, they are often incomplete in their spatial or temporal  
12 coverage. Satellite measurements of aerosol optical depth (AOD) have much broader  
13 temporal and spatial coverage, and have also been used to constrain BC sources  
14 [Huneeus et al., 2003; Xu et al., 2013]. However, AOD reflects the contribution from  
15 all aerosol components, making it difficult to distinguish and quantify different  
16 aerosol species, especially their relative fractions.

17 The OMI aerosol absorption optical depth (AAOD), the non-scattering part of the  
18 AOD, is an atmospheric column measurement of absorbing aerosol particles, i.e.,  
19 absorbing carbon and mineral dust, which provides a different perspective to  
20 constrain BC sources [Torres et al., 1998; Koch et al., 2009]. In this study, the  
21 GEOS-Chem adjoint model and satellite observations of OMI AAOD are used to  
22 constrain spatially resolved BC emissions. Our study focuses on April and October to

1 compare seasons when the dust loading over Southeast Asia is relatively large and  
2 small. Section 2 describes the observations, emissions, and forward and inverse model  
3 used in this study. Then we quantify discrepancies between observations and model  
4 estimates based on different BC anthropogenic emissions in Section 3. Section 4  
5 describes how formulation of the inverse problem affects the results; evaluation of the  
6 inversion results with different prior emission inventories and independent  
7 observations are presented in Section 5, and we end with discussion and conclusions  
8 in Section 6.

## 10 **2. Data and Models**

### 11 **2.1 Observations**

#### 12 **2.1.1 OMI AAOD**

13 The Ozone Monitoring Instrument (OMI) aboard Aura is a nadir-viewing, wide-swath  
14 hyper-spectral imaging spectrometer that provides daily global coverage with high  
15 spectral resolutions and spatial resolution of  $13 \times 24 \text{ km}^2$  at nadir [Levelt et al.,  
16 2006a]. It detects backscattered solar radiance in the ultraviolet-visible wavelengths  
17 (0.27 to 0.5  $\mu\text{m}$ ) to measure aerosols, clouds, surface UV irradiance, and trace gases  
18 [Levelt et al., 2006b]. OMI takes advantage of the greater sensitivity of radiances  
19 measured at the top-of-atmosphere in the near-UV region to the varying load and type  
20 of aerosols to derive extinction AOD, single scattering albedo (SSA), and AAOD  
21 using an inversion procedure at 354, 388 and 500 nm generated by the near-UV  
22 (OMAERUV) algorithm [Torres et al., 2007]. The optical depths at 388 nm are

1 inverted from radiance observations while the 354 and 500 nm results are obtained by  
2 conversion of the 388 nm retrievals. The OMAERUV retrieval algorithm is  
3 particularly sensitive to carbonaceous and mineral aerosols. It assumes that the  
4 column aerosol load can be represented by one of three types of aerosols and uses a  
5 set of aerosol models to account for the presence of these aerosols: carbonaceous  
6 aerosol from biomass burning, desert dust, and weakly absorbing sulfate-based  
7 aerosols. Each aerosol type is represented by seven aerosol models of varying single  
8 scattering albedo, for a total of twenty-one models. The twenty-one aerosol models  
9 used by OMAERUV are based on long-term statistics of ground-based observations  
10 by the AERONET. The major factor affecting the quality of aerosol products is sub-  
11 pixel cloud contamination, while AAOD is probably less affected by cloud  
12 contamination due to a partial cancellation of cloud effects on the retrieved AOD  
13 and SSA co-albedo. Due to the large sensitivity of OMI near UV observations to  
14 particle absorption, AAOD is the most reliable quantitative OMAERUV aerosol  
15 parameter, especially over land. The root-mean-square error for AAOD is estimated to  
16 be  $\sim 0.01^1$ . In this study, we used the OMAERUV Level-2 aerosol data product, which  
17 includes the quality assurance flag, thus only the most reliable retrievals minimally  
18 affected by sub-pixel cloud contamination are used [Ahn et al., 2014]. Important  
19 algorithm improvements have been implemented in the current OMAERUV  
20 algorithm. The carbonaceous aerosol model was replaced with a new model that  
21 accounts for the presence of OC while the previous aerosol model only assumed black

---

<sup>1</sup>[daac.gsfc.nasa.gov/Aura/data-holdings/OMI/documents/v003/OMAERUV\\_README\\_V003.doc](https://daac.gsfc.nasa.gov/Aura/data-holdings/OMI/documents/v003/OMAERUV_README_V003.doc)

1 carbon as the absorbing component [Jethva and Torres, 2011]. In the revised  
2 algorithm, the identification of aerosol type has been improved by taking advantage  
3 of the Atmospheric Infrared Sounder (AIRS) carbon monoxide (CO) observations in  
4 conjunction with OMI UV-AI. The aerosol layer height (ALH) value is taken from a  
5 climatology derived from CALIOP (Cloud-Aerosol Lidar with Orthogonal  
6 Polarization) observations specifically produced for this purpose [Torres et al., 2013].  
7 The Level 2 OMI AAOD data reports a set of retrieved parameters for different  
8 assumptions of the altitude of the aerosol center of mass: at the surface, and at 1.5,  
9 3.0, 6.0 and 10.0 km above the surface [Torres et al., 2005]. A best-guess set of  
10 retrieved values of AOD, AAOD and SSA associated with the climatological ALH  
11 value from the CALIOP-based climatology is reported as the standard OMAERUV  
12 aerosol product. When the aerosol layer height is not available from CALIOP  
13 climatology, the height is obtained as in the previous version of the algorithm based  
14 on a climatology of GOCART model simulated aerosol heights. For carbonaceous and  
15 desert dust particles, the aerosol load is assumed to be vertically distributed following  
16 a Gaussian function characterized by peak (aerosol layer height) and half-width  
17 (aerosol layer geometric thickness) values [Torres et al., 2005; Torres et al., 2013].  
18 The retrieval values of AAOD are much larger if using the aerosol layer altitude  
19 where more absorbing aerosols are loaded. In general, when comparing satellite  
20 retrievals of trace gases with other measurements or model simulations, it is essential  
21 to take into account the different sensitivities of the instruments by applying  
22 averaging kernels [Luo et al., 2007; Worden et al., 2007]. However, there is no



1 averaging kernel for OMI AOD/AAOD retrievals. It is thus important to consider  
2 differences in aerosol properties and distributions used in the retrieval algorithm with  
3 those in the assimilation model (e.g., GEOS-Chem). The retrieval “Final AAOD”  
4 products (OMI\_Final) are interpolated values using the aerosol layer height value  
5 given by the CALIOP climatology [Torres et al., 2013].

6 OMAERUV retrievals of AOD and SSA have been evaluated by comparison to  
7 independent ground-based observations provided by the world-wide Aerosol Robotic  
8 Network (AERONET). OMAERUV AOD retrievals at 380 nm were compared to  
9 AERONET observations [Ahn et al., 2014]. Over 10,000 matched OMAERUV-  
10 AERONET AOD pairs at 44 globally distributed land-locations were analyzed. The  
11 AERONET-OMAERUV analysis reported a high level of agreement between the two  
12 datasets, yielding a correlation coefficient of 0.81, y-intercept of 0.1, and slope of  
13 0.79. Sixty five percent of the analyzed OMAERUV AOD data agreed with  
14 AERONET measurements within OMAERUV’s stated uncertainty (largest of 0.1 or  
15 30%). The OMAERUV SSA product has also been evaluated using AERONET  
16 retrievals. Jethva et al [2014] compared OMAERUV and AERONET SSA retrievals  
17 using all available AERONET data at 269 sites for the 2005-2013 period. After  
18 accounting for the wavelength difference (AERONET’s 440 nm versus OMAERUV’s  
19 388 nm), it was shown that 50% of the satellite SSA retrievals agree with  
20 AERONET’s values within 0.03, whereas 75% of the matched pairs agree within 0.05  
21 for all aerosol types. The most important source of uncertainty is the effect of sub-  
22 pixel cloud contamination, related to the sensor’s coarse spatial resolution, which

1 causes AOD and SSA overestimates for cases of low aerosol load, and severely limits  
2 the overall retrieval yield of the algorithm.

3 In order to obtain a consistent vertical profile between the OMI retrieval and GEOS-  
4 Chem, we use the GEOS-Chem simulated aerosol layer height instead of the  
5 CALIOP-based aerosol layer height climatology to calculate a GEOS-Chem-based  
6 observed AAOD (referred as OMI\_GC AAOD) as a linear interpolation of the OMI  
7 observed AAOD values corresponding to different assumed peak heights. Figure 1  
8 shows the differences between OMI\_Final and OMI\_GC AAOD over Southeast Asia  
9 for April and October 2006. In April, the enhancements from applying the GEOS-  
10 Chem aerosol layer height are quite significant, with 30-50% increases over eastern  
11 China and downwind areas while 20-30% increases over India and southeastern Asia,  
12 since the simulated aerosol layer heights are much lower than those based on  
13 CALIOP. The increases even exceed 60% across broad areas over the tropical ocean.  
14 Some reductions are shown over parts of western China and northern Asia in the  
15 OMI\_GC AAOD. In October, the patterns of enhancement and reduction are similar  
16 to those in April, with smaller changes (less than 20%) over broad continental areas.  
17 The most significant differences occur near the major aerosol source regions, such as  
18 eastern China and South Asia. We also evaluate the linearity of the relationship  
19 between aerosol layer height and AAOD from OMI retrievals. We find (not shown)  
20 that there is less than 30% error in linearly interpolating AAOD corresponding to a  
21 specific aerosol layer height from the AAODs corresponding to two other aerosol  
22 layer heights.

### 1    **2.1.2 AERONET AAOD**

2    The Aerosol Robotic Network (AERONET) is a ground-based instrument network  
3    providing a long-term, continuous and readily accessible public domain database of  
4    aerosol optical, microphysical and radiative properties [Holben et al., 1998].  
5    AERONET inversion code provides aerosol optical properties (including size  
6    distribution, refractive index, and single scattering albedo) in the total atmospheric  
7    column derived from the direct and diffuse radiation measured by Cimel sun/sky-  
8    radiometers [Dubovik and King, 2000; Dubovik et al., 2000, 2002a, 2002b; Dubovik  
9    et al., 2006; Sinyuk et al., 2007].

10   We use Level 2.0 quality-assured AERONET aerosol inversions data of AAOD at 440  
11   nm. The prefield and postfield calibrations have been applied in these measurements  
12   and they were cloud cleared and manually inspected [Omar et al., 2013]. The total  
13   uncertainty in the AERONET AOD for field instruments is  $\pm 0.1$  to  $\pm 0.2$  and is  
14   spectrally dependent with the higher errors ( $\pm 0.2$ ) in the UV spectral range [Eck et al.,  
15   1999]. The retrieved single scattering albedo uncertainties are within 0.03, estimated  
16   by Dubovik et al., [2000], with the exception of the 0.44  $\mu\text{m}$  retrievals for the desert  
17   dust case when they increase by  $\sim 0.09$  and 0.07 for low and high aerosol loadings,  
18   respectively [Sinyuk et al., 2007]. In this study, only the AAOD data corresponding to  
19   AOD values greater than 0.4 are include.

### 20   **2.1.3 In situ measurements**

21   For the monthly surface BC observation over Southeast Asia, we combine the in situ  
22   measurements of BC concentration based on several published studies [Zhang et al.,

1 2008; Beegum et al., 2009; Moorthy et al., 2013]. Over China, the monthly surface  
2 BC concentrations are from 12 sites, including urban sites and rural sites for April and  
3 October, 2006, which were based on results of Zhang et al. [2008]. The locations of  
4 these 12 sites are shown in Fig. 2. The BC concentrations are analyzed using thermo-  
5 chemical analysis from PM<sub>10</sub> aerosols, which were collected by air sample [Zhang et  
6 al., 2008]. The daily BC measurements are only available at the site of Xi'an (XIA).  
7 The PM<sub>2.5</sub> BC concentrations were measured continuously as 5-min averages by  
8 quartzfiber filter tape transmission at an 880 nm wavelength with an aethalometer  
9 [Hansen et al., 1984]. More details about the measurement methods are described in  
10 Cao et al. [2007; 2009].

11 The measurements of monthly surface BC concentrations for 2006 using  
12 aethalometers over India were based on Beegum et al. [2009] and Moorthy et al.  
13 [2013], which were carried out in eight sites covering India and adjacent oceanic  
14 regions. Locations of these sites are indicated in Fig. 2. More details about the  
15 measurements and sites are described by Beegum et al. [2009]. DEL and KGP  
16 represent urban and semi-urban sites in the Indo-Gangetic Plain (IGP). HYD and  
17 PUN represent urban locations. TVM is a semi-urban coastal station in the south  
18 India; NTL is a high altitude location in the central Himalayas, and MCY and PBR  
19 are two island locations representing the Arabian Sea and Bay of Bengal, respectively.

## 20 **2.2 GEOS-Chem**

21 GEOS-Chem is a global three-dimension chemical transport model driven by  
22 assimilated meteorological observations from the Goddard Earth Observing System

1 (GEOS) of the NASA Global Modeling and Assimilation Office (GMAO) [Bey et al.,  
 2 2001]. We use the nested-grid GEOS-Chem model [Wang et al., 2004; Chen et al.,  
 3 2009] driven by GEOS-5 meteorological fields with 6-hour temporal resolution (3-  
 4 hour for surface variables and mixing depths),  $0.5^\circ$  (latitude)  $\times$   $0.667^\circ$  (longitude)  
 5 horizontal resolution over the window of Southeast Asia ( $70^\circ\text{E}$ – $150^\circ\text{E}$ ,  $11^\circ\text{S}$ – $55^\circ\text{N}$ ),  
 6 and 47 vertical layers between the surface and 0.01 hPa. A global simulation with  
 7 lower resolution of  $4^\circ$  (latitude)  $\times$   $5^\circ$  (longitude) provides the lateral boundary  
 8 conditions to the higher resolution nested-grid simulation every 3 hours.

9 The original carbonaceous aerosol simulation in GEOS-Chem was developed by Park  
 10 et al. [2003]. It assumes that 80% of BC and 50% of OC emitted from primary  
 11 sources are hydrophobic and that hydrophobic aerosols become hydrophilic with an e-  
 12 folding time of 1.15 days [Park et al., 2003; Chin et al., 2002; Cooke et al., 1999].

13 Dust in GEOS-Chem is distributed across four size bins (radii 0.1– 1.0, 1.0–1.8, 1.8–  
 14 3.0, and 3.0–6.0  $\mu\text{m}$ ) following Ginoux et al. [2004]. The smallest size bin is further  
 15 divided equally into four sub-micron size bins (with effective radii centered at 0.15,  
 16 0.25, 0.4 and 0.8 $\mu\text{m}$ ) for calculation of optical properties and heterogeneous  
 17 chemistry [Fairlie et al., 2010; Ridley et al., 2012]. Due to the significant positive  
 18 biases identified in GEOS-Chem dust simulations both in surface concentration and  
 19 dust AOD [Fairlie et al., 2010, Ku and Park, 2011; Ridley et al., 2012; Wang et al.,  
 20 2012], a new emitted dust particle size distribution (PSD) based upon scale-invariant  
 21 fragmentation theory [Kok, 2011] with constraints from in situ measurements [Zhao  
 22 et al., 2010] is implemented in GEOS-Chem to improve the dust simulation [Zhang et

1 al., 2013]. Large discrepancies are reduced between the simulated surface-level fine  
 2 dust concentration and measurements from the IMPROVE network in the western US  
 3 during March to May of 2006 [Zhang et al., 2013]. The new PSD also improves the  
 4 positive biases of AOD over the Asian and African dust source region in April 2006  
 5 (See Fig. S1 in supplemental). The wet deposition scheme [Liu et al., 2001] includes  
 6 scavenging in convective updrafts as well as in-cloud and below-cloud scavenging  
 7 from convective and large-scale precipitation. Dry deposition is based on the  
 8 resistance-in-series scheme of Wesely [1989] as implemented by Wang et al. [1998].  
 9 The aerosol optical depth at 400 nm is calculated online assuming log-normal size  
 10 distributions of externally mixed aerosols and is a function of the local relative  
 11 humidity to account for hygroscopic growth [Martin et al., 2003]. The AAOD of each  
 12 aerosol species is calculated as [Ma et al., 2012; Cohen and Wang, 2014; Cohen,  
 13 2014]

$$14 \qquad \qquad \qquad \text{AAOD} = \text{AOD} * (1 - \text{SSA}) \qquad \qquad \qquad (1),$$

15 where SSA is the single scattering albedo.

### 16 **2.3 BC Emission Inventories**

17 Emissions of BC from biomass burning sources are taken from version 2 of the GFED  
 18 8-day inventory [van der Werf et al., 2006; Randerson et al., 2006]. GFED v2 is  
 19 derived using satellite observations of active fire counts and burned areas in  
 20 conjunction with the Carnegie-Ames-Stanford-Approach (CASA) biogeochemical  
 21 model. Carbon emissions are calculated as the product of burned area, fuel load and  
 22 combustion completeness. Burned area is derived using the active fire and 500-meter

1 burned area datasets from the Moderate Resolution Imaging Spectroradiometer  
2 (MODIS) as described by Giglio et al. [2006]. We also use a newer version of GFED  
3 v3 daily emissions for sensitivity analysis [van derWerf et al., 2010]. Compared to  
4 GFED v2, the main update in GFED v3 is the spatial resolution of the global grid is  
5 quadrupled from 1° to 0.5°, the native 500-m MODIS daily burned area maps are  
6 applied [Giglio et al., 2010], the regional regression trees of GFEDv2 are replaced by  
7 a local regression approach in producing the indirect, active-fire based estimates of  
8 burned area, and a revised version of Carnegie-Ames Stanford Approach (CASA)  
9 biogeochemical model is used.

10 Global anthropogenic emissions for carbonaceous aerosols (BC/OC) in GEOS-Chem  
11 are originally from Bond et al. [2004, 2007], which contain both biofuel and fossil  
12 fuel emissions. The estimated BC emissions uncertainties are -36% to 149% over  
13 China and 38% to -119% for India [Bond et al., 2004; Lu et al., 2011]. In this study,  
14 we evaluate three additional carbonaceous anthropogenic emission inventories over  
15 Southeast Asia and China: the Streets regional inventory for Intercontinental  
16 Chemical Transport Experiment - Phase B (INTEX-B), the Southeast Asia  
17 Composition, Cloud, Climate Coupling Regional Study (SEAC<sup>4</sup>RS) emission  
18 inventory, and the Multi-resolution Emission Inventory for China (MEIC,  
19 <http://www.meicmodel.org/>). Anthropogenic emissions are all classified into four  
20 major sectors: power generation, industry, residential and transport. The INTEX-B  
21 inventory is based on 2006 and contains monthly variations with 0.5° × 0.5°  
22 horizontal resolution over Southeast Asia (Zhang et al., 2009). The SEAC<sup>4</sup>RS

1 inventory is an annual, finer resolution inventory based on 2012, with  $0.1^\circ \times 0.1^\circ$   
2 horizontal resolution over Southeast Asia [Lu et al., 2011]. The average uncertainties  
3 of BC are estimated to be  $-43\%$  to  $90\%$  over China, which are much lower than those  
4 of the INTEX-B between  $-68\%$  to  $308\%$  [Zhang et al., 2009; Lu et al., 2011]. The  
5 MEIC emission inventory over China also includes monthly variations and is  
6 provided at the  $0.5^\circ \times 0.5^\circ$  horizontal resolution. These four anthropogenic emission  
7 inventories are regridded to the GEOS-Chem resolution of  $0.5^\circ \times 0.667^\circ$ , and their  
8 annual emissions are shown in Fig. 3. The differences in these inventories exceed  
9  $100\%$  across broad areas, especially over India and eastern China. The anthropogenic  
10 emission inventory of INTEX-B is comparable to that of MEIC over eastern China  
11 while lower than that of Bond and SEAC<sup>4</sup>RS over western China and India. Both  
12 Bond and SEAC<sup>4</sup>RS inventories are lower over central and eastern China compared to  
13 those of INTEX-B and MEIC inventories. With much finer resolution, the SEAC<sup>4</sup>RS  
14 emission inventory indicates more hot spots spread across eastern and central China  
15 and the IGP and eastern India where rural population densities are high and residential  
16 coal and biofuel combustion are prevalent [Lu et al., 2011].

#### 17 **2.4 GEOS-Chem Adjoint and Inverse Modeling**

18 An adjoint model is a set of equations auxiliary to a forward model that are used to  
19 efficiently calculate the gradient of a scalar model response function with respect to  
20 all model parameters simultaneously [Lions, 1971]. The adjoint of GEOS-Chem was  
21 developed specifically for inverse modeling including explicit treatment of gas-phase  
22 chemistry, heterogeneous chemistry, black and organic primary aerosol, as well as the



1 treatment of the thermodynamic couplings of the sulfate-ammonium-nitrate-formation  
 2 chemistry [Henze et al., 2007; 2009], with code updates following the relevant parts  
 3 of the GEOS-Chem forward model up through version v9. The GEOS-Chem adjoint  
 4 model has been developed and widely used to constrain sources of emission such as  
 5 dust [Wang et al., 2012], ammonia [Zhu et al., 2013], CO [Kopacz et al., 2009;  
 6 Kopacz et al., 2010; Jiang et al., 2011], CH<sub>4</sub> [Wecht et al., 2012; Wecht et al., 2014],  
 7 and to investigate pollution transport [e.g., Zhang et al., 2009, Kopacz et al., 2011].

8 The 4D variational data assimilation technique is used with the GEOS-Chem  
 9 adjoint model to combine observations and models to calculate an optimal estimate of  
 10 emissions. A range of emissions are constructed using control variables,  $\sigma$ , to adjust  
 11 the vector of model emissions via application as scaling factors with elements  $\sigma = \frac{E}{E_a}$ ,  
 12 where  $E$  and  $E_a$  are posterior and prior BC emission vectors, respectively. This  
 13 method of inverse modeling seeks  $\sigma$  that minimizes the cost function,  $J$ , presented  
 14 by:

$$22 \quad J = \frac{1}{2} \sum_{c \in \Omega} (Hc - c_{obs})^T S_{obs}^{-1} (Hc - c_{obs}) + \frac{1}{2} \gamma_r (\sigma - \sigma_a)^T S_a^{-1} (\sigma - \sigma_a) \quad (2),$$

15 where  $c$  is the vector of species concentrations mapped to the observation space by  $H$ ,  
 16 the observation operator,  $c_{obs}$  is the vector of species observations,  $\sigma_a$  is the prior  
 17 estimate of the scaling factors,  $S_{obs}$  and  $S_a$  are error covariance estimates of the  
 18 observations and scaling factors, respectively, and  $\Omega$  is the domain over which  
 19 observations are available. The first term of the cost function in Eq. (2) is the  
 20 observation term, which is the total prediction error incurred for departure of model  
 21 predictions from the observations. The second term, the a priori term or penalty

1 (background) term, is the penalty incurred for departure from the prior emissions.  
 2 Here  $\mathbf{S}_a$  is assumed to be diagonal, and the significance of the prior information is  
 3 more of a smoothness constraint than a rigorous estimate of prior uncertainty  
 4 [Rodgers, 2000].  $\gamma_r$  is a regularization parameter, which used to balance the two terms  
 5 [Hansen 1998; Henze et al., 2009]. We will discuss the contributions of the penalty  
 6 term in Section 4.2.  
 7 Overall, the minimum value of the cost function balances the objectives of improving  
 8 model performance while ensuring the model itself remains within a reasonable range  
 9 (as dictated by  $\mathbf{S}_a^{-1}$ ) of the initial model. The minimum of the cost function is sought  
 10 iteratively using the quasi-Newton L-BFGS-B algorithm [Zhu et al., 1994; Byrd et al.,  
 11 1995]. This approach requires the gradients of the cost function with respect to the  
 12 emission scaling factors at each iteration, which are calculated with the GEOS-Chem  
 13 adjoint model.

## 14 **2.5 Cost function and adjoint forcing**

15 OMI\_GC AAOD column observations represent the combined absorption of all  
 16 aerosols species (dominated by BC, dust, and to a lesser extent OC). Similarly,  
 17 modeled total column AAOD,  $\mathbf{T}_{GC}$ , is the sum of modeled column absorption from  
 18 BC ( $\mathbf{T}_{GC\_BC}$ ), OC ( $\mathbf{T}_{GC\_OC}$ ) and dust ( $\mathbf{T}_{GC\_Dust}$ ):

$$19 \quad \mathbf{T}_{GC} = \mathbf{T}_{GC\_BC} + \mathbf{T}_{GC\_OC} + \mathbf{T}_{GC\_Dust} \quad (3).$$

20 In order to use AAOD observations to develop constraints on BC alone, we must  
 21 formulate the observation term of the cost function to isolate the impacts of BC on the  
 22 difference between simulated and observed AAOD. Here we consider four

1 approaches: methods (a) – (d). The first two methods use modeled ratios of BC to  
 2 total absorption (either in each layer (a), or the total column (b)) to derive an  
 3 “observed” BC AAOD. Method (c) makes a direct comparison between total AAOD  
 4 in the model and measurements. Lastly, in method (d), we also consider using a  
 5 subset of the OMI data that has been flagged in the retrieval process as being  
 6 impacted by carbonaceous aerosol. These different approaches to constructing a cost  
 7 function, and the gradient of these cost functions with respect to the vertically  
 8 resolved modeled BC concentration (i.e., the adjoint forcing) are presented below.  
 9 Here we do not consider the penalty term in the cost function in order most clearly  
 10 assess how formulation of the observation term impacts the inversion. The  
 11 consequences of the different cost function formulations are described in Section 4.1.

12 (a): In this method, the observation term of the cost function can be written as:

$$13 \quad \mathcal{J} = \frac{1}{2} \sum_i^N \sum_{l=1}^L (\tau_{GC\_BC,l,i} - \tau_{OMI\_BC,l,i})^2 * S_{OMI,i}^{-2} \quad (4),$$

14 where  $L$  is the top of atmosphere,  $N$  is the total number of observations, and  $\tau_{GC\_BC,l,i}$   
 15 and  $\tau_{OMI\_BC,l,i}$  are the modeled and observed BC AAODs at layer  $l$  for the  $i^{th}$   
 16 observation, respectively. The latter is calculated for any  $i$  from the OMI column  
 17 AAOD ( $T_{OMI,i}$ ) using the ratio of vertically resolved BC AAOD to column AAOD in  
 18 the prior model,

$$19 \quad \tau_{OMI\_BC,l,i} = T_{OMI,i} \frac{\tau_{GC\_BC,l,i}^a}{T_{GC,i}^a} \quad (5),$$

20 where superscript  $a$  indicates the prior model estimates. Since the ratio  $\frac{\tau_{GC\_BC,l,i}^a}{T_{GC,i}^a}$  is a  
 21 constant throughout the inversion, the  $i^{th}$  adjoint forcing is

$$\frac{\partial \mathcal{J}}{\partial BC_1} = \frac{\partial \tau_{GC\_BC,i}}{\partial BC_1} * \left( \tau_{GC\_BC,i} - T_{OMI,i} \frac{\tau_{GC\_BC,i}^a}{T_{GC,i}^a} \right) * S_{OMI,i}^{-2} \quad (6).$$

(b) In this method, the cost function is based on BC AAOD column differences:

$$\mathcal{J} = \frac{1}{2} \sum_i^N (T_{GC\_BC,i} - T_{OMI\_BC,i})^2 * S_{OMI,i}^{-2} \quad (7).$$

The observed BC AAOD column is calculated from the OMI\_GC AAOD column and the ratio of modeled column BC AAOD to total column AAOD from the prior simulation:

$$T_{OMI\_BC,i} = T_{OMI,i} \frac{T_{GC\_BC,i}^a}{T_{GC,i}^a} \quad (8).$$

The  $i^{th}$  adjoint forcing is thus

$$\frac{\partial \mathcal{J}}{\partial BC_1} = \frac{\partial \tau_{GC\_BC,i}}{\partial BC_1} * \left( T_{GC\_BC,i} - T_{OMI,i} \frac{T_{GC\_BC,i}^a}{T_{GC,i}^a} \right) * S_{OMI,i}^{-2} \quad (9).$$

(c) The observation term of the cost function can be written in terms of total column absorption as:

$$\mathcal{J} = \frac{1}{2} \sum_i^N (T_{GC,i} - T_{OMI,i})^2 * S_{OMI,i}^{-2} \quad (10).$$

In this case, the adjoint forcing is

$$\frac{\partial \mathcal{J}}{\partial BC_1} = \frac{\partial \tau_{GC\_BC,i}}{\partial BC_1} * (T_{GC\_BC,i} + T_{GC\_OC,i} + T_{GC\_Dust,i} - T_{OMI,i}) * S_{OMI,i}^{-2} \quad (11).$$

(d) The OMI OMAERUV retrievals algorithm also flags instances for which the retrieval algorithm relied upon the presence of carbonaceous aerosols. Using only these retrievals, the observation term of the cost function can be written in terms of the direct difference between simulated columns BC AAOD and BC flagged OMI AAOD observations:

$$\mathcal{J} = \frac{1}{2} \sum_i^N (T_{GC\_BC,i} - T_{OMI\_BC\_Flag,i})^2 * S_{OMI\_BC,i}^{-2} \quad (12).$$

1 where  $T_{\text{OMI\_BC\_Flag}}$  is the OMI AAOD flagged for the presence of carbonaceous  
 2 aerosols ( $\text{OMI\_GC\_AAOD\_BC}$ , which is different than Eq. 5 or 8 which depend upon  
 3 prior model ratios). In this case, the gradient of the cost function with respect to BC  
 4 concentration at the layer  $l$  will be

$$5 \quad \frac{\partial J}{\partial \text{BC}_l} = \frac{\partial \tau_{\text{GC\_BC},l}}{\partial \text{BC}_l} * (T_{\text{GC\_BC},l} - T_{\text{OMI\_BC\_Flag},l}) * S_{\text{OMI\_BC},l}^{-2} \quad (13).$$

6 The implications of the different cost function formulations will be described in  
 7 Section 4.1.

### 8 **3 Impacts of BC anthropogenic emission uncertainties**

9 In this section, we quantify the extent to which differences in anthropogenic emission  
 10 inventories contribute to uncertainties in simulated surface BC and AAOD. Here, the  
 11 SEAC<sup>4</sup>RS emission inventory is appended to the MEIC emission inventory outside of  
 12 China for the Southeast Asian nested simulation ( $\text{MEIC\_SEAC}^4\text{RS}$ ). Figure 4 shows  
 13 the impact of different BC anthropogenic emission inventories on simulated surface  
 14 BC concentrations and comparisons to in situ measurements over China [Zhang et al.,  
 15 2008, Cao et al., 2009]. The monthly and daily ground-based measurements at sites  
 16 representative of four different regions are shown: northern China (Gucheng, GUC),  
 17 northeastern China (Longfengshan, LFS), southern China (Nanning, NAN), and  
 18 midwestern China (XiAn, XIA). Generally, the modeled and observed BC  
 19 concentrations are higher in winter than in summer. In addition to enhanced  
 20 anthropogenic emissions during the winter [Fu et al., 2012], the Asian summer  
 21 monsoon plays an important role in this seasonal cycle by reducing aerosol  
 22 concentrations in the summer over China [Zhang et al., 2010]. Though the model

1 simulation is able to capture the seasonal variability, it underestimates surface BC  
2 concentration at the urban sites, such as GUC, NAN, and XIA, with all of these  
3 anthropogenic emission inventories, except at NAN, where the SEAC<sup>4</sup>RS inventory  
4 leads to values as high or higher than observed, but the seasonal variation has not yet  
5 been reproduced. With the INTEX-B and MEICS inventory, though the surface BC  
6 concentrations are underestimated at some background and rural sites [Fu et al., 2012;  
7 Wang et al., 2013], the simulated BC surface concentrations at the rural site of LFS  
8 are quite comparable to the observation, especially the seasonal variations. The  
9 INTEX-B and MEIC inventories improve the BC concentrations in winter with the  
10 inclusion of monthly variability over China compared to the inventories of Bond and  
11 SEAC<sup>4</sup>RS.

12 The spatial distributions of simulated surface BC concentrations using  
13 MEIC\_SEAC<sup>4</sup>RS and INTEX-B inventories are compared to the in situ observation at  
14 20 sites over Southeast Asia for April and October 2006 in Fig. 5. The east to west  
15 gradient in China and the north to south gradient in India are not well reproduced by  
16 the model, where the simulated BC concentrations are much lower over eastern China  
17 and the IGP for both April and October, especially for the urban areas since the model  
18 is unable to resolve individual urban hot spots [Fu et al., 2012].

19 Figure 6a shows the differences in monthly average AAOD between the model using  
20 the MEIC\_SEAC<sup>4</sup>RS inventory and OMI (former minus latter) for April and October  
21 2006. GEOS-Chem underestimates AAOD compared to OMI across broad areas of  
22 Southeast Asia in April, especially eastern China and the IGP. In October, AAOD is

1 underpredicted over northern China while it is over predicted over eastern China and  
2 most of South Asia. Corresponding OMI data counts towards the monthly average at  
3 each grid cell are shown in Fig. 6b. In general, more data are available over northern  
4 China and India. We note that the data counts are much lower in October compared to  
5 April over southern China and the Indo China Peninsular, where the observations are  
6 overestimated. Sparse OMI observations over these areas may result in apparent high  
7 or low biases. If we only take into account the OMI\_GC AAOD\_BC retrievals, the  
8 differences and corresponding OMI data counts for April and October are shown in  
9 Fig. 7. The spatial distributions are quite similar to those using all AAOD  
10 observations shown in Fig. 6, but with much larger negative differences over Asia in  
11 April and over northern China and IGP in October. The data counts are also smaller  
12 when only considering the OMI\_GC AAOD\_BC observations, especially over the  
13 dust source regions and downwind areas in April and broad areas over South Asia in  
14 October.

15 We also compared the observed to simulated AAOD using different emission  
16 inventories (figures not shown here). The simulated AAOD is comparable using  
17 INTEX-B and MEIC emission inventories over eastern China, while it is much lower  
18 than the OMI column retrieval using the inventories of Bond and SEAC<sup>4</sup>RS. With the  
19 SEAC<sup>4</sup>RS inventories, the simulated AAOD over the IGP shows enhancements  
20 compared to that using Bond and INTEX-B inventories.

## 21 **4. Uncertainties of observation and penalty terms**

### 22 **4.1 Adjoint forcing**

1 As described in Section 2.5, there are four methods to formulate the observation term  
2 of the cost function owing to different approaches of deriving an “observed” BC  
3 AAOD. We perform sensitivity experiments to quantify the impact of using these  
4 different formulations. For these tests, only the observation term is considered in the  
5 cost function (i.e., the penalty term is not included), and we use the same  
6 anthropogenic emission inventory (MEIC\_SEAC<sup>4</sup>RS) as the prior emissions for each  
7 test. Figure 8 shows the results of the differences between optimized and prior  
8 anthropogenic BC emissions based on the four approaches.

9 Qualitatively, there are many noticeable differences between the optimization results  
10 using the different formulations of the observation operator. In April, enhanced  
11 anthropogenic BC emissions are shown over broad areas using all four methods.  
12 However, slight reductions appear over eastern China and southern India when using  
13 method (b), (c) and (d). In particular, method (c) results in lower posterior emissions  
14 over China. The results of methods (c) and (d) are quite consistent except the  
15 enhancements of posterior emissions over southern India occur using method (d).

16 Similarly, although the four optimized patterns are quite consistent in October, much  
17 larger areas of BC emissions reduction result from using method (c). The reductions  
18 of method (d) are similar to that of method (c) over eastern China, while quite  
19 different over India with significantly enhanced posterior emissions.

20 The differences in results are related to different assumptions implicit in the various  
21 forms of the cost function considered. Both method (a) and method (b) depend on the  
22 relative ratio of BC to other absorbing aerosol (e.g. dust, OC) in the model. Further,



1 method (a) introduces a stronger dependency on the GEOS-Chem prior vertical  
2 distribution, since the observation operator includes three dimensions with all vertical  
3 layers, compared to the column based method (b). Since there are more observations  
4 over IGP and northeastern China in April, this stronger constraint may enhance the  
5 negative forcing due to the model underestimation, which leads to increasing  
6 emissions. Since, through the adjustment of the OMI data to generate the OMI\_GC  
7 product, we have already used the GEOS-Chem prior information on the aerosol  
8 vertical distribution, it seems preferable to adopt a column-based approach for the  
9 assimilation. Though both method (b) and method (c) are based on the column  
10 AAOD, the former assumes that the relative contributions of BC to total AAOD in the  
11 model is correct, while the latter assumes that absolute contributions of OC and dust  
12 are correct. The simulated total AAOD might not be equivalent to the observed  
13 AAOD after optimization in both method (a) and method (b) since the adjoint forcing  
14 only accounts for the BC AAOD. In addition, the results would highly depend on the  
15 model performance in simulating the ratio between BC and other absorbing aerosol.  
16 There are no significant biases for the GEOS-Chem simulated fraction of coarse model  
17 dust mass [Wang et al., 2012, Philip et al., 2014], which suggests that the simulated  
18 dust AAOD fraction is likely unbiased. However the simulated mass of both BC and  
19 OC in GEOS-Chem are biased low [Heald et al., 2005; Fu et al., 2012]. We thus  
20 adopt method (c), since the strength of the adjoint forcing with respect to BC sources  
21 depends upon the BC absolute contribution in AAOD rather than the relative  
22 contribution of method (b), which may have less model dependency in simulating the

1 distribution of other aerosols. The major differences between method (c) and method  
2 (d) are the available observation data counts, as the data counts of the latter are much  
3 fewer than the former. In April, the pattern of optimized emissions using method (c)  
4 and method (d) are quite consistent, suggesting that BC AAOD play a dominant role  
5 in contributing to the total AAOD. We will adopt method (c) for the following  
6 experiments and also discuss method (d) in section 5.4 for comparison.

#### 7 **4.2 Penalty Term**

8 The inclusion of a penalty, or background term, in the cost function is a key factor for  
9 inverse modeling. It is specified through the prior (background) error covariance  
10 matrix,  $\mathbf{S}_a$ , and a regularization parameter  $\gamma_r$ . In the absence of rigorous statistical  
11 information on the error covariance of the emissions, we assume the errors are  
12 uncorrelated and use an L-curve selection criterion to identify an optimal value of  $\gamma_r$   
13 [Hansen, 1998; Henze et al., 2009]. The uncertainties of BC are assumed to be 100%  
14 of the maximum BC emissions over the simulation domain. Thus, the optimal values  
15 of  $\gamma_r$  are selected to be 0.5 for April and 1.0 for October based on the  
16 MEIC\_SEAC<sup>4</sup>RS emission and the cost function in Eq. (10). The contribution of the  
17 penalty term results in smaller adjustments to emissions, as the regularized results  
18 prefer smoother solutions than those of the unconstrained inversion tests in Fig. 8.  
19 Here we assume a single constant value for  $\mathbf{S}_a$  along the diagonal and no off-diagonal  
20 terms.

21

### 22 **5. Analysis of Optimizations**

1 We next proceed to constrain Southeast Asian BC sources using OMI\_GC AAOD.  
2 The OMI\_GC AAOD observations are compared to model estimates from GEOS-  
3 Chem nested simulation for April and October 2006 using the difference between  
4 simulated total AAOD and observed OMI\_GC AAOD (i.e., Eq. (10)). Tens of  
5 thousands of OMI retrievals per month are available for the assimilation, but not all of  
6 the retrievals are usable. In the presence of cirrus clouds, retrievals errors are  
7 significant. The effect of optically thin cirrus is similar to that of subpixel cloud  
8 contamination. As plumes of dust or smoke aerosol drift away from their source  
9 regions, they become mixed with clouds. This problem is particularly evident over the  
10 oceans, which are frequently covered with thin cirrus and fair-weather cumulus  
11 clouds. Generally, the retrieved AAOD shows a reduced coverage especially over the  
12 oceans due to cloud contamination and the effects of sun glint [Torres et al., 2007].  
13 Thus, quality and diagnostic flags are defined to classify and filter the retrievals. In  
14 October, only observations north of 5°N are included for data assimilation to  
15 minimize contributions of biomass burning from Indonesian fires.

## 16 **5.1 Optimized emissions**

17 Considering the performances of the four emission inventories discussed in Section  
18 2.3, the following optimized results will mainly focus on using the MEIC\_SEAC<sup>4</sup>RS  
19 and INTEX-B inventories. The prior and posterior (optimized) BC emissions from  
20 anthropogenic sources are shown in Fig. 9. Overall, the results show an enhancement  
21 in BC emissions over broad areas of Southeast Asia, with adjustments that are  
22 seasonally and spatially heterogeneous. This is consistent with the top-down

1 constraints on BC emissions based on ground-base measurements by Fu et al., [2012],  
2 which also show that the BC emissions are greatly enhanced across broad areas of  
3 China, in particular northern and central China and the megacity clusters. In April,  
4 either using MEIC\_SEAC<sup>4</sup>RS or INTEX-B inventories, large increases of up to a  
5 factor of 3-5 are shown after optimization. The largest enhancements occur sharply in  
6 eastern China and the IGP in April by up to a factor of five (Fig. 9). Other large  
7 increases are located in South Asia, northeastern and northwestern China. There is a  
8 small decrease in anthropogenic BC in part of southwestern China. That is quite  
9 different from the inversion results based on AOD by Xu et al. [2013], wherein the  
10 optimized anthropogenic BC emissions are reduced by 9.1% over China, even though  
11 the prior BC anthropogenic emissions that they used are from Bond et al., [2004,  
12 2007], which much lower than what we used. The dust scheme had not yet been  
13 updated and modified in Xu et al., [2013] following the revised particle size  
14 distribution suggested in Zhang et al. [2013]. Thus it is possible that overestimated  
15 dust and AOD projected a model bias onto adjustments of emissions of all type of  
16 aerosols over dust regions and downwind areas, such as eastern China. Considering  
17 the dust season in April, we also perform a sensitivity experiment to quantify the  
18 uncertainty of dust impacts on the inversion results by doubling the dust emission in  
19 April. The general pattern of the optimized anthropogenic BC emissions are  
20 consistent with that of the standard inversion, with a maximum differences less than  
21 20%.  
22 However, the adjustments of anthropogenic BC emissions before and after

1 optimization in October are different than those in April (Fig. 10). The optimization of  
2 anthropogenic emissions yields a slight reduction (1~5%) over central India and part  
3 of southern China and an increase by 10~50% over eastern and northern China, as  
4 well as northwestern India.

5 Though the adjusted patterns of optimized BC emission are basically comparable by  
6 using MEIC\_SEAC<sup>4</sup>RS and INTEX-B inventories, significant differences are located  
7 over India and eastern China (Fig. 11). We also note that the differences in the  
8 optimized results are almost the same as those of the prior emissions between  
9 MEIC\_SEAC<sup>4</sup>RS and INTEX-B inventories. The ratio between their posterior  
10 differences and prior differences (see Fig. 11, right column) shows that the  
11 optimization increases their differences, relative to the prior, over broad areas over  
12 China and India up to a factor of three in April, with only slight decreases over south  
13 India. In October, optimization decreases the posterior differences between  
14 MEIC\_SEAC<sup>4</sup>RS and INTEX-B emission inventories relative to the prior by 10-20%  
15 over southern and most of India. Areas where prior differences are increased/reduced  
16 are consistent with the areas where the emissions increase/decrease after optimization  
17 (see Fig. 10). This suggests that absolute errors in the prior emissions may be larger  
18 than the relative prior uncertainty percentages considered here.

19 In addition to reducing the bias of the emissions, it is important to consider how much  
20 the inversion has reduced uncertainty in the emissions. A new method based on the  
21 Broyden-Fletcher-Goldfarb-Shanno (BFGS) algorithm is used to estimate the  
22 posterior uncertainty [Bousserez et al., 2014]. The posterior error reductions are up to

1 30% and 15% in April and October over the IGP and eastern China, where the  
2 anthropogenic emission enhancements were the largest (Figure 9 and 10). The prior  
3 errors do not change across broad areas, where the changes of optimized emissions  
4 are relatively smaller.

5 While the most substantial adjustments are made to anthropogenic emissions, biomass  
6 burning emission are also adjusted. The most significant increases are over South  
7 Asia and Eastern Europe in April, especially, the indo-China peninsula and eastern  
8 Russia (figures not shown). The optimized biomass burning emissions in October  
9 have the largest enhancements are over south Borneo and Sumatra. Similar to the  
10 optimized anthropogenic emission, there is also not much change for the optimized  
11 biomass burning emission throughout India and and indo-China peninsula in October.  
12 To examine the impacts of different prior anthropogenic inventories on optimized  
13 biomass burning emissions, we consider the following ratios:

$$14 \quad \frac{\Delta MEIC\_SEAC4RS_{GFED3} - \Delta MEIC\_SEAC4RS_{GFED2}}{GFED3 - GFED2} \quad (14).$$

15 Eq. 14 shows how changes in anthropogenic emissions during the optimization  
16 compare when using two different biomass burning inventories, relative to the  
17 difference in these biomass burning inventories themselves. Large values of this ratio  
18 indicate regions where our top-down constraints on anthropogenic emissions are more  
19 sensitive to errors in the prior biomass burning inventories, such as over eastern China  
20 and the southern IGP (Fig. 12).

## 21 **5.2 Optimized BC AAOD**

22 The largest uncertainty reductions are obtained over eastern China and the IGP, so

1 here we consider AAOD in these regions alone. Fig. 13 shows the observed and  
2 simulated BC AAOD over eastern China (105°-125°E, 20°-45°N) before and after  
3 optimization in green along with linear line slope equation and correlation  $R^2$ . Here  
4 the observed BC AAOD is derived from the OMI\_GC AAOD and the prior ratio of  
5 simulated BC AAOD versus total AAOD. The prior BC AAOD is misrepresented and  
6 underestimated compared to observation over eastern China, especially in April. The  
7 low biases of the prior slopes are improved after optimization in April and October by  
8 132% and 11%, respectively. Similar to the optimized BC concentrations, the  
9 improvements in October after optimization are less significant than in April. There  
10 are only slight changes in correlation coefficients, which may due to the large number  
11 of samples in both spatial and temporal dimensions across which variations are not in  
12 the same directions. In the IGP area, which we define as (70°-90°E, 23°-32°N), the  
13 low biases of prior BC AAOD are much larger than those in eastern China (Fig. 14).  
14 The values of most observed BC AAOD are lower than 0.3 and the slopes are 0.22  
15 and 0.28 in April and October. After optimization, the slope increase by 155% and the  
16 correlation coefficients change from 0.2 to 0.25 in April. In October, there is a 32%  
17 increase in slope and the correlation coefficient doubles but still remains small (from  
18 0.06 to 0.12).  
19 Though slopes improve after optimization for both eastern China and India, they still  
20 show considerable lower biases. This results, in part, from constraints of the penalty  
21 term. Additionally, we note that many prior AAOD values are very small and close to  
22 zero. These are hard for the optimization routine to adjust significantly in the areas

1 where the values of prior emission are very small or close to zero. Since the  
 2 optimization scheme is based on the use of emissions scaling factors, large gradients  
 3 with respect to BC concentrations will result in small gradients with respect to  
 4 emissions scaling factors in locations with small emissions. To test how much this  
 5 formulation restricts the inversion, a sensitivity experiment was performed assuming  
 6 uniform prior emissions in all grid boxes. This facilitates adjustments to prior  
 7 emissions throughout the domain, resulting in larger posterior AAOD after  
 8 optimization. However, the resulting spatial distributions and gradients of  
 9 anthropogenic emissions are not realistic (e.g., large emissions are not placed in  
 10 known source areas). Alternatively, instead of adjusting emissions through application  
 11 of scaling factors,  $\sigma$ , to the a priori emissions, the BC emissions themselves could be  
 12 treated as the control variables in the cost function (Eq. 15). Another sensitivity  
 13 experiment is performed for April 2006, inverting for the emissions themselves rather  
 14 than the emissions scaling factors. Figure S2 in supplemental shows the total  
 15 emissions (summed across sectors) after optimization using different inversion  
 16 approaches. Fig. S2a is result based on the scaling factor as describe by Eq. 2 in  
 17 Section 2.4 that the range of emissions are constructed using scaling factors as control  
 18 variables to adjust the vector of model emissions. Fig. S2b shows the results when  
 19 emissions are constrained directly as the control variables in the penalty term as:

$$20 \quad J = \frac{1}{2} \sum_{c \in \Omega} (Hc - c_{obs})^T S_{obs}^{-1} (Hc - c_{obs}) + \frac{1}{2} \gamma_r (E - E_a)^T S_a^{-1} (E - E_a) \quad (15).$$

21 This formulation allows the inversion to place significant emissions in areas where  
 22 the prior emissions are very small or close to zero. The optimized emissions over the



1 larger prior source areas, such as northeastern China and the middle IGP, are smaller  
2 than when optimizing scaling factors. These sensitivity tests demonstrate the value of  
3 using the prior emissions inventories, either explicitly or implicitly through scaling  
4 factors, in terms of constraining the magnitude of known sources, and the downside in  
5 terms of the difficulty in introducing new sources through the inversion.

6 We also evaluate (Fig. 15) the prior and posterior simulated AAOD against the OMI  
7 and AERONET daily average AAOD at 4 sites where there are available  
8 measurements during the periods of April and October, 2006 (see the red sites in Fig.  
9 2): Beijing (BJ) in China, Kanpur (KP) and Gandhi\_College (GH) in India, and  
10 Mukdahan (MD) in Thailand. The daily average GEOS-Chem model results and  
11 OMI\_GC AAOD are sampled according to the AERONET observations at the  
12 locations of the 4 sites. At the Beijing site, the prior model AAOD estimates driven  
13 either by MEIC\_SEAC<sup>4</sup>RS or INTEX-B inventories are underestimated by a factor of  
14 ~2, while the posterior AAOD are more comparable to the observations in April. In  
15 terms of temporal variability, the model is able to capture some features of peaks after  
16 optimization. At the two sites in India, only a few measurements are available in late  
17 April, but the magnitudes are close to OMI observation. The optimized results using  
18 the MEIC\_SEAC<sup>4</sup>RS inventory shows great improvements compared to the prior  
19 AAOD. However, the optimized AAOD using the INTEX-B inventory still shows  
20 negative biases. The differences in optimized AAOD between using INTEX-B and  
21 MEIC\_SEAC<sup>4</sup>RS come from their prior differences in AAOD. This again  
22 demonstrates that the posterior optimization results are not independent of the prior

1 emission inventories, consistent with the estimated reduction in posterior error shown  
2 in Fig 10. At the site of Gandhi\_College (GH) and Mukdahan (MK) there are large  
3 differences between the OMI and AERONET AAODs; the magnitudes of the  
4 OMI\_GC AAODs are much lower than those from AERONET, even close to zero on  
5 some days. Koch et al. [2009] compared the AERONET and OMI retrievals of AAOD  
6 at AERONET sites. The results showed that the two retrievals broadly agree with  
7 each other, but that the OMI\_GC AAOD is much smaller over Asia. In our study, only  
8 a few OMI observed AAOD pixels are available in Thailand site (MK) (Fig. 6); these  
9 limited and sparse observations do not provide enough information to robustly  
10 constrain emissions in this region.

### 11 **5.3 Optimized surface BC concentrations**

12 As mentioned before, the prior surface BC concentrations are underestimated in most  
13 of the urban and rural sites over China. Figure 16 shows the spatial distribution of  
14 optimized surface BC concentrations compared to in situ measurements at 20 sites in  
15 Southeast Asia. The largest in situ BC concentrations observed over eastern China  
16 and the IGP, which are densely populated, industrialized areas, are now reproduced  
17 well by the optimized simulation. After optimization, the spatial gradients of the  
18 observed BC concentrations are captured by the model: high in the east and low in the  
19 west for China, and high in the north and low in the south for India. Using the  
20 MEIC\_SEAC<sup>4</sup>RS inventory for the prior emissions, the optimized spatial distributions  
21 are better simulated than when than using the INTEX-B inventory. In particular, the  
22 simulated BC concentrations are much closer to the observations over the IGP after

1 optimization. The performance of simulated surface BC concentrations in the WRF-  
2 Chem (Weather Research and Forecasting model coupled with Chemistry) model with  
3 GOCART aerosol scheme using our optimized INTEX-B inventory has also been  
4 tested for April 2006 (see supplemental Fig. S3). A low bias using the prior INTEX-B  
5 inventory have been significantly reduced, and the simulated surface BC  
6 concentrations have increased by a factor of 1.5-2 in April 2006. The scatter plots in  
7 Fig. 17 show the correlations of BC concentrations from surface observations and  
8 GEOS-Chem before (blue) and after (red) optimization. Initial negative biases are  
9 shown in both April and October. The linear regression slope increases by more than  
10 a factor of four in April. However, the modeled BC concentrations at most of the sites  
11 only change slightly after the optimization in October, which results in a much  
12 smaller improvement in the regression slope (21%). The correlation coefficients  
13 increase by 0.04 to 0.08 after optimization; such small improvement may be owing to  
14 the sparse spatial distributions of the observational sites.

15 More specific site-by-site comparisons between model and observations are shown in  
16 Fig. 18. Although the optimized BC surface concentrations are enhanced in April,  
17 overestimation occurs in some eastern sites in China. The overestimates of optimized  
18 surface BC concentrations at XIA, GUC and TYS (Fig. 18a) are possibly attributed to  
19 the underestimate of absorbing OC and associated brown carbon, the latter which is  
20 not included in the model. In October, the low biases are corrected both in the urban  
21 sites and rural sites, especially the eastern rural sites in China. However, there is a  
22 persistent negative bias in most sites after optimization in October. Due to the very

1 low prior emissions, the optimization has less impact on the western sites in China.  
2 The GEOS-Chem prior simulation underestimates surface BC concentrations in all  
3 the urban sites and coastal sites over India in April (Fig. 5). While the optimization  
4 enhances the BC sources and surface concentration, it still shows a negative bias in  
5 most of sites over India, especially the urban sites. The smaller improvement in  
6 coastal sites is not only due to the low prior emissions but also the large uncertainties  
7 of AAOD retrieval for low aerosol amounts over the ocean.  
8 Given the stark contrast between the inversion results in April and October, we also  
9 conducted the optimization for two additional months in winter (January) and summer  
10 (July) season using MEIC\_SEAC<sup>4</sup>RS as the prior inventory. In January, the  
11 anthropogenic emissions show enhancements over the IGP and parts of western and  
12 northern China and slight decreases over southern India and eastern and southern  
13 China (figures not shown here), which results in increasing the surface BC  
14 concentrations in XIA and LFS sites while decreasing concentrations in the sites of  
15 GUC and NAN (see Fig. 4). In July, there is no significantly change for the surface  
16 BC concentrations after optimization owing to very sparse observation in July over  
17 eastern China. From this seasonal comparison, it appears that the BC anthropogenic  
18 emissions are not always underestimated during the year. The largest  
19 underestimations across the whole region of Southeast Asia occur in April. The  
20 underestimated regions are mainly over IGP and northern China in both January and  
21 October. The slight overestimates are indicated over southern India and part of  
22 eastern China in January as well as northern China in July.

1 Discrepancies versus surface observations might also relate to model representational  
2 error incurred by comparing ~50 km gridded estimates to in situ BC measurements,  
3 which likely have finer length-scales of variability [Wang et al., 2013; Cohen and  
4 Prinn, 2011; Cohen et al., 2011]. Considering the coarse resolution of the model  
5 when comprising with the ground-based measurements, we investigate the impacts of  
6 model resolution by considering approaches for downscaling the model simulations.  
7 One approach is to use high-resolution population datasets to redistribute primary  
8 aerosol concentrations [e.g., Krol et al., 2005; UNEP, 2011; Silva et al., 2013]. Based  
9 on a finer resolution population density dataset, a parameterization of the urban  
10 increment for non-reactive primary emitted anthropogenic BC and organic matter has  
11 been developed and tested for coarse resolution air quality model. This method does  
12 not alter concentrations at rural sites since it assumes that results at coarse resolution  
13 only represent the rural (background) sites. According to this method, we used a high-  
14 resolution ( $1/24^\circ \times 1/24^\circ$ ) population dataset of Gridded Population of the World,  
15 Version 3 (GPWv3, [http://sedac.ciesin.columbia.edu/data/set/gpw-v3-population-](http://sedac.ciesin.columbia.edu/data/set/gpw-v3-population-density-future-estimates)  
16 [density-future-estimates](http://sedac.ciesin.columbia.edu/data/set/gpw-v3-population-density-future-estimates)) to downscale and adjust the simulated BC concentration at  
17 urban sites (defined locations where population density exceeding  $600/\text{km}^2$ ). The  
18 scatter plots (Fig. 17b) show that, on average, the application of population  
19 downscaling improves the performance of the modeled results compared to the non-  
20 adjusted BC concentrations in April for both the prior and posterior simulations,  
21 although low biases remain in each. It does not make any change in the slope in  
22 October after applying the population parameterization, and correlation is degraded.

1   Downscaled estimates at only two sites (LIA and NAN) show enhancements, and the  
2   rest are not impacted.

3   To more directly investigate the impact of model resolution, it would be ideal to  
4   compare the results of the present simulations to higher resolution simulations with  
5   the same model [e.g., Punger and West, 2013]. While this is not currently an option  
6   for this model version, we can conduct GEOS-Chem simulations at a coarser  
7   resolution ( $2^\circ$  latitude  $\times$   $2.5^\circ$  longitude) and make inferences about the role of  
8   resolution errors. Fig. 19 shows the resolution errors in estimated surface BC  
9   concentrations in the coarse resolution results ( $2^\circ \times 2.5^\circ$ ) with respect to fine  
10   resolution simulations ( $0.5^\circ \times 0.667^\circ$ ). The resolution error exceeds 20% across broad  
11   areas, and even up to 300% over the IGP and part of Southeastern Asia. The surface  
12   BC concentrations are much lower using coarse resolution over the major source  
13   regions, in particular the IGP, where the resolution error is more than 3. This is likely  
14   owing to coarse grid boxes not describing the sharp gradient between high  
15   concentrations in the valley and low concentrations in the mountain. The optimized  
16   surface BC concentrations from our  $0.5^\circ \times 0.667^\circ$  simulations are underestimated by a  
17   factor of 2-3 at the IGP sites compared to in situ measurements. Punger and West  
18   [2013] show that the percent difference between all-cause mortality estimates at 12  
19   km resolution and at coarser resolutions of 36 km and 96 km for BC is ~9% and  
20   ~23%, respectively. Assuming that model skill at estimating variations in  
21   concentrations at the scales of the in situ measurements is similar to that for  
22   estimating exposure based on highly resolved populations distribution, we can

1 extrapolate from the results of Pungner and West [2013] that the resolution errors in the  
2  $0.5^{\circ} \times 0.667^{\circ}$  simulation, relative to the scale of the measurements, is a bit less than the  
3 resolution error in the  $2^{\circ} \times 2.5^{\circ}$  simulation relative to the  $0.5^{\circ} \times 0.667^{\circ}$  simulation  
4 Thus, the former may be as large as a factor of  $\sim 2.5$  in individual grid cells.

#### 5 **5.4. Comparisons using OMI\_GC AAOD\_BC**

6 A subset of the OMI retrievals (OMI\_GC AAOD\_BC) are flagged during the retrieval  
7 process as being indicative of the presence of carbonaceous aerosols. Using only  
8 these retrievals for the inversion, the differences between prior and posterior (later  
9 minus former) BC anthropogenic emissions using MEIC\_SEAC<sup>4</sup>RS inventory are  
10 shown in Fig. 20. Compared to Fig. 9 and Fig. 10, there are similar signs of emissions  
11 adjustments over most of Southeast Asia, except in October over India where  
12 reductions are not shown in the posterior emissions due to fewer available  
13 observations in the OMI\_AAOD\_BC data subset. Moreover, the magnitudes of  
14 enhanced emissions in April are much larger if we use only the OMI\_GC AAOD\_BC  
15 retrievals. This also results in larger posterior surface BC concentrations (figures not  
16 shown) in some area and AAOD that improve the underestimates in a few sites when  
17 compared to the ground-base measurements and AERONET observation. However,  
18 the differences are not obvious in October and the improvements in April are neither  
19 significant nor widespread. Considering there are fewer observations available using  
20 OMI\_GC AAOD\_BC, especially in October and other summer month (e.g. July), and  
21 that it does not change the major conclusions compared to using OMI\_GC AAOD,  
22 using OMI\_GC AAOD is recommended.

1

## 2 **6. Summary and Discussions**

3 In this study, we used space-based observations of absorbing aerosol optical depth  
4 (AAOD) from the OMI instrument to constrain BC monthly average emissions for  
5 April and October, 2006, with the GEOS-Chem model and its adjoint. First, we  
6 evaluated the model simulated BC concentrations using four different anthropogenic  
7 emission inventories. The differences in these inventories exceeded 100% across  
8 broad areas of Southeast Asia. For each of the four emission inventories, the  
9 simulated surface BC concentrations had low biases compared to the available surface  
10 observations in most urban sites in Southeast Asia.

11 The adjoint model was used to perform 4D-Var inverse modeling to constrain BC  
12 emissions. After optimization, both anthropogenic and biomass burning emissions  
13 were adjusted. Either using the MEIC\_SEAC<sup>4</sup>RS or INTEX-B inventory, the  
14 optimized anthropogenic emissions for BC were significantly enhanced over broad  
15 areas of Southeast Asia in April compared to the prior emission, with the largest  
16 enhancements in eastern China and India IGP of up to a factor of five. From analysis  
17 of inversions using different prior biomass burning inventories it was shown that  
18 optimized anthropogenic emissions were most sensitive to the prior biomass burning  
19 over eastern China and southern IGP. The adjustments in October were smaller than  
20 those in April. Inverse modeling in additional months indicated that BC  
21 anthropogenic emissions were not always underestimated throughout the year. The  
22 largest underestimates occurred in April throughout Southeast Asia. Only slight



1 overestimates were indicated over southern India and eastern China for both January  
2 in July. Inversion results were in general similar using either all OMI observed  
3 AAOD or just the OMI\_GC AAOD\_BC. In October, the posterior anthropogenic  
4 emissions yielded a slight reduction (1~5%) over central India and part of southern  
5 China while they increased by 10~50% over eastern and northern China, as well as  
6 northwestern India. The uncertainty of the posterior emissions over the IGP and  
7 eastern China were estimated to have reduced by up to 30% and 15% in April and  
8 October. Although April is the dust season in Asia, the impact of doubling dust  
9 emissions on the posterior anthropogenic emissions is less than 20%.

10 After optimization, the model's low biases for BC AAOD improved by 132% and  
11 11% over Southeast Asia in April and October, respectively. In eastern China, these  
12 improvements were more significant (143% and 30% in April and October). The  
13 remaining residual error in the simulated AAOD, which was significant in October,  
14 particularly in India, may be a consequence of the inverse modeling framework,  
15 which had difficulty introducing emissions in locations where the prior emissions  
16 were close to zero. This downside may be overcome by performing inversions  
17 directly for the emissions, rather than emissions scaling factors.

18 Results of the inversion were also compared to remote and in situ measurements that  
19 were not assimilated. The posterior modeled AAOD were quite comparable to  
20 AERONET AAOD observations in April in China; however, large discrepancies  
21 persisted at the sites over India and Thailand after data assimilation. These residual  
22 errors may be associated with the limited and sparse observations of OMI AAOD in

1 these regions, which themselves were not very consistent with AERONET AAOD.

2 Jethva et al., [2014] also pointed out that much of the inconsistency of SSA between

3 OMI and AERONET is observed at moderate to lower aerosol loading (AOD

4  $440\text{nm} < 0.7$ ) for which both inversion techniques might have errors related to small

5 signal-to-noise and algorithmic assumptions. Low biases of surface BC

6 concentrations were improved or corrected at urban sites and eastern rural sites over

7 China in April, with the linear regression slope between model and observed values

8 increasing by more than a factor of four. However, the adjustments were not strong

9 enough in most sites over India in April and October nor over China in October.

10 Moreover, the optimization had less impact on the western sites in China and coastal

11 sites in India due to the very low prior emissions and the large uncertainties in AAOD

12 retrieval for low aerosol amounts over the ocean. Model resolution error was also an

13 important factor contributing to discrepancies of BC concentrations compared to in

14 situ measurements. Comparison to coarser model simulations and the results of

15 Punter and West [2013] indicates that resolution errors may be up to a factor of 2.5 in

16 grid cells in regions such as the IGP and part of southeastern Asia. Nevertheless, the

17 results found here are not exclusively germane to GEOS-Chem, as we find that

18 implementing the optimized INTEX-B inventory in WRF-Chem improved simulated

19 surface BC concentrations by a factor of 1.5-2 relative to simulations with the prior

20 INTEX-B inventory.

21 Overall, this work was the first attempt to formally use the absorbing aerosol products

22 from satellite observation for a BC emissions inversion. Both the simulated AAOD

1 and surface BC concentration showed significant improvements spatially and  
2 temporally after data assimilation, especially in April. However, there were still  
3 several sources of uncertainty and limitations of this work worth considering. Aspects  
4 such as model error and assumptions made regarding the observations and  
5 uncertainties in the observations and prior emissions inventories contributed greatly to  
6 uncertainties in the optimization results.

7 Our assumption that errors in the prior emissions were only 100% restricted the  
8 magnitude of the emissions adjustments allowed by the inversion. One might  
9 conclude that such restrictions were too strict; however, uncertainties in emissions  
10 were also not likely the only source of the discrepancy between observed and  
11 predicted BC concentrations and AAOD. Textor et al. [2007] noted that inter-model  
12 differences were only partially explained by differences in emission inventories;  
13 removal processes also play an important role in affecting the lifetime and  
14 concentrations of BC in the free troposphere. Although the 1 day aging from  
15 hydrophobic BC to hydrophilic BC in GEOS-Chem is typical for this type of model  
16 [Koch et al., 2009], aerosol internal mixing that includes effects of various physical,  
17 chemical, and meteorological processing can also significantly impact BC  
18 concentrations and aerosol absorptions [Stier et al., 2006; Cohen and Prinn 2011;  
19 Cohen et al., 2011; Buchard et al., 2014], in some cases even more so than  
20 uncertainties in emissions [Shen et al., 2014]. The scheme used in our study for  
21 aerosol scavenging was based on Liu et al., [2001], which did not distinguish between  
22 rain and snow. The recent updates by Wang et al. [2011] included corrections to

1 below-cloud and in-cloud scavenging that improved the overestimation of integrated  
2 scavenging [Dana and Hales, 1976]. Corresponding updates to the wet scavenging in  
3 the GEOS-Chem adjoint might also be helpful for improving the optimized results.  
4 The optimizations were sensitive to how model information was used to calculate the  
5 BC component of the measured AAOD, which alone provided only a constraint on the  
6 column concentrations of all absorbing aerosol (i.e., including dust and OC). We  
7 have adjusted the OMI observed AAOD by applying the GEOS-Chem simulated  
8 aerosol layer height to reduce the differences in the vertical profiles between the  
9 model and observation, referred to as OMI\_GC AAOD. However, there could be  
10 inconsistent treatment of microphysical and optical properties used in the AAOD  
11 calculation between the model and OMI retrievals. The results of the optimization  
12 may be biased by error in the model's vertical distribution of BC, which has been  
13 adjusted in other studies [van Donkelaar et al., 2013]. To evaluate the magnitude of  
14 this potential source of error, we also repeated the inversions using the OMI retrieval  
15 based on the CALIOP and GOCART aerosol layer height. The difference in the  
16 optimized anthropogenic BC emissions are less than 30% in April and 10% in  
17 October compared to inversions using OMI\_GC AAOD.

18 It is important to realize that BC from most emission sources contains not only  
19 elemental and organic fractions [Chow et al., 2009], but also non-soot OC, i.e., brown  
20 carbon, that has a significant absorbing component at short wavelengths comparable  
21 to elemental carbon absorption [Jacobson, 1999; Kirchstetter et al., 2004; Andreae  
22 and Gelencser, 2006; Hoffer et al., 2006; Magi et al., 2009]. However, absorbing

1 aerosols in GEOS-Chem only include BC, OC and dust, while the brown carbon has  
2 not yet been taken into account. Therefore, in this study, the simulated BC is  
3 effectively a proxy of all absorbing carbonaceous aerosols, and the resulting  
4 constraints on emissions are thus best interpreted as constraints on absorbing  
5 carbonaceous emissions. While the attribution of ambient aerosol absorption to BC may  
6 be a reasonable approximation in areas dominated by fresh soot emissions, it may lead to  
7 misleading estimates of the AAOD when other light absorbing particles were present  
8 since the so-called brown carbon contributes 28% on average of the total absorption at  
9 440 nm [Bahadur et al., 2012]. This undoubtedly resulted in overestimation of BC  
10 emissions after optimization in areas where brown carbon was a component of the  
11 observed AAOD. We performed a sensitivity experiment by removing 30% of the  
12 total absorption from the OMI AAOD observation, since GEOS-Chem does not  
13 include brown carbon. The optimized anthropogenic emissions are lower by up to  
14 30% over the major source regions compared to the standard results. Given that the  
15 model has large low biases of surface OC concentrations over eastern China [Fu et al.,  
16 2012], the overestimated BC concentrations after optimization at XIA, GUC and TYS  
17 (Fig. 18a) may possibly be attributed to the underestimation of absorbing OC (brown  
18 carbon).

19 Lastly, it is well known that the quality of the observation data plays a critical role in  
20 data assimilation. Although the OMI observed AAOD retrieval provided much better  
21 spatial and temporal coverage than remote sensing measurements such as AERONET,  
22 we noted that there were large discrepancies between OMI\_GC AAOD and

1 AERONET observation in some areas, especially in October (see Fig. 15). The  
2 OMAERUV retrievals were typically more reliable over land than over water since  
3 the ocean surface reflectance shows distinct angular and spectral variations. The  
4 major factor affecting the quality of the OMI aerosol product was sub-pixel cloud  
5 contamination due to the relatively large footprint of the OMI observations [Torres et  
6 al., 1998]. Satheesh et al. [2009] demonstrated the potential of multi-satellite analysis  
7 of A-train data to improve the accuracy of retrieved aerosol products and suggested  
8 that a combined OMI-MODIS-CALIPSO retrieval had potential to further improve  
9 assessments of aerosol absorption, which would possible enhance the observation  
10 quality in data assimilation. Recently, other improvements include the development of  
11 CALIOP-based aerosol layer height climatology and the use of AIRS carbon  
12 monoxide real-time observations to distinguish smoke from dust aerosol, which  
13 improved the retrieval performance by 5-20% [Torres et al., 2013]. Using the updated  
14 OMAERUV when it becomes available will likely improve the optimization results in  
15 future work.

#### 16 **Acknowledgement.**

17 This work was supported from Environmental Protection Agency-STAR grant RD-  
18 83503701-0. Although the research described in the article has been funded wholly or  
19 in part by the U.S. EPA's STAR program through grant (RD-83503701-0), it has not  
20 been subjected to any EPA review and therefore does not necessarily reflect the views  
21 of the Agency, and no official endorsement should be inferred. We thank the OMI  
22 team ([http://disc.sci.gsfc.nasa.gov/Aura/data-holdings/OMI/omaeruv\\_v003.shtml](http://disc.sci.gsfc.nasa.gov/Aura/data-holdings/OMI/omaeruv_v003.shtml))

1 and AERONET team ([http://aeronet.gsfc.nasa.gov/cgi-bin/webtool\\_opera\\_v2\\_inv](http://aeronet.gsfc.nasa.gov/cgi-bin/webtool_opera_v2_inv)) for  
2 providing the data and establishing and maintaining the sites used in this study.

3

#### 4 **Figure captions.**

5

6 **Figure 1.** Absolute and relative differences in AAOD between OMI\_Final and  
7 OMI\_GC AAOD for April and October 2006.

8

9 **Figure 2.** Twenty sites of ground measurements (black dots) and four sites of  
10 AERONET observation (red cross dots). Also shown are terrain heights (color shaded  
11 contours, unit: m).

12

13 **Figure 3.** Annual anthropogenic emission of BC regridded into GEOS-Chem  
14 resolution of  $0.5^{\circ} \times 0.667^{\circ}$  from the inventories of (a) Bond, (b) INTEX-B, (c)  
15 SEAC<sup>4</sup>RS, and (d) MEIC.

16

17 **Figure 4.** Comparison of the observed and simulated surface BC concentrations using  
18 four emission inventories at the site of GUC, LFS, NAN, XIA. The orange dots are  
19 the monthly mean posterior surface BC concentrations at these sites using MEIC  
20 inventory over China.

21

22 **Figure 5.** Spatial distributions of prior surface BC concentrations using INTEX-B and  
23 MEIC\_SEAC<sup>4</sup>RS inventories overlaid with BC in situ measurements of 20 sites.

24

25 **Figure 6.** (a) Differences of monthly average AAOD between model using  
26 MEIC\_SEAC<sup>4</sup>RS inventory and the OMI observation (former minus latter) and (b)  
27 corresponding OMI monthly data in each grid cell for April and October 2006.

28

29 **Figure 7.** The same as Figure 6, but for OMI\_AAOD\_BC.

30

31 **Figure 8.** Differences between optimized and prior anthropogenic BC emissions  
32 based on four methods of adjoint forcing (a) vertically resolved BC AAOD base on  
33 model, (b) column BC AAOD based on model, (c) column total OMI\_GC AAOD and  
34 (d) column OMI\_GC AAOD\_BC for April and October 2006.

35

36 **Figure 9.** Anthropogenic BC emissions for April 2006. The first column shows the  
37 prior inventory, the second is the optimized inventory, the third is the differences  
38 between the prior and optimization, and the last column is the relative changes of  
39 posterior error, based on the inventories of (a) INTEX-B and (b) MEIC\_SEAC<sup>4</sup>RS.

40

- 1 **Figure 10.** The same as Figure 9, but for October 2006.
- 2
- 3 **Figure 11.** Differences of anthropogenic BC emissions between using the inventories  
 4 of MEIC\_SEAC<sup>4</sup>RS and INTEX-B for April and October 2006. The left column  
 5 shows the prior inventory, the center is the optimized inventory, and right column is  
 6 the ratio between their posterior differences and prior differences.
- 7
- 8 **Figure 12.** The sensitivities of optimized anthropogenic emission based on GFED2  
 9 and GFED3 relative to the differences between GFED2 and GFED3.
- 10
- 11 **Figure 13.** Comparison of BC AAOD over eastern China (105°-125°E, 20°-45°N)  
 12 between OMI measurements and GEOS-Chem before and after the assimilation for  
 13 April and October 2006.
- 14
- 15 **Figure 14.** Comparison of BC AAOD over IGP (70°-90°E, 23°-32°N) between OMI  
 16 measurements and GEOS-Chem before and after the assimilation for April and  
 17 October 2006.
- 18
- 19 **Figure 15.** Comparison of total daily AAOD from OMI, AERONET and GEOS-  
 20 Chem before and after the data assimilation at the four AERONET sites for April and  
 21 October 2006.
- 22
- 23 **Figure 16.** Spatial distributions of optimized surface BC concentrations using  
 24 INTEX-B and MEIC\_SEAC<sup>4</sup>RS inventories overlaid with BC in situ measurements  
 25 of 20 sites.
- 26
- 27 **Figure 17.** Comparison of monthly surface BC concentration for April and October  
 28 2006, between in situ measurements and GEOS-Chem before and after the  
 29 assimilation (a) without and (b) with population density downscaling.
- 30
- 31 **Figure 18.** Comparison of monthly surface BC concentration between in situ  
 32 measurements and GEOS-Chem over (a) China and (b) India before and after the  
 33 assimilation using the inventories of MEIC\_SEAC<sup>4</sup>RS and INTEX-B for April and  
 34 October 2006.
- 35
- 36 **Figure 19.** The resolution errors of surface BC between the simulations of coarse  
 37 resolution (2°x2.5°) and fine resolution (0.5°x0.667°).
- 38
- 39 **Figure 20.** The differences between the prior and posterior anthropogenic BC  
 40 emissions for April and October 2006, using OMI\_GC AAOD\_BC as the observation.
- 41
- 42
- 43 **References**
- 44 Ackerman, A. S., Toon, O. B., Stevens, D. E., Heymsfield, A. J., Ramanathan, V., and



1        Welton, E. J.: Reduction of tropical cloudiness by soot, *Science*, 288(5468),  
2        1042–1047, doi:10.1126/science.288.5468.1042, 2000.

3        Ahn, C., Torres, O., and Jethva, H.: Assessment of OMI near-UV aerosol optical  
4        depth over land, *J. Geophys. Res. Atmos.*, 119, 2457–2473,  
5        doi:10.1002/2013JD020188, 2014.

6        Andreae, M. O. and Gelencsér, A.: Black carbon or brown carbon? The nature of  
7        light-absorbing carbonaceous aerosols, *Atmos. Chem. Phys.*, 6, 3131–3148,  
8        doi:10.5194/acp-6-3131-2006, 2006.

9        Bahadur, R., Praveen, P. S., Xu, Y., and Ramanathan, V.: Solar absorption by  
10        elemental and brown carbon determined from spectral observations, *P. Natl.*  
11        *Acad. Sci. USA*, 109, 17366–17371, doi:10.1073/pnas.1205910109, 2012.

12        Beegum, S. N., Moorthy, K. K., Babu, S. S., Satheesh, S.K., Vinoj, V., Badarinath,  
13        K.V.S., Safai, P.D., Devara, P.C.S., Singh, S., Vinod, Dumka, U.C., Pant, P.:  
14        Spatial distribution of aerosol black carbon over India during pre-monsoon  
15        season, *Atmos. Environ.*, 43(5), 2009, 1071–1078, 2009.

16        Bey, I., Jacob, D. J., Yantosca, R. M., Logan, A. J., Field, B., Fiore, A. M., Li, Q., Liu,  
17        H., Mickley, L. J., and Schultz, M.: Global modeling of tropospheric chemistry  
18        with assimilated meteorology: Model description and evaluation, *J. Geophys.*  
19        *Res.*, 106, 23,073–23,095, 2001

20        Bond, T. C. and Bergstrom, R. W.: Light absorption by carbonaceous particles: An  
21        investigative review, *Aerosol Sci. Tech.*, 40, 27–67, 2006.

22        Bond, T. C., Bhardwaj, E., Dong, R., Jogani, R., Jung, S. K., Roden, C., Streets, D.  
23        G., and Trautmann, N. M.: Historical emissions of black and organic carbon  
24        aerosol from energy-related combustion, 1850–2000, *Glob. Biogeochem. Cy.*, 21,  
25        Gb2018, doi:10.1029/2006GB002840, 2007

26        Bond, T. C., Doherty, S. J., Fahey, D. W., Forster, P. M., Berntsen, T., DeAngelo, B.  
27        J., Flanner, M. G., Ghan, S., Kärcher, B., Koch, D., Kinne, S., Kondo, Y., Quinn,  
28        P. K., Sarofim, M. C., Schultz, M. G., Schulz, M., Venkataraman, C., Zhang, H.,  
29        Zhang, S., Bellouin, N., Guttikunda, S. K., Hopke, P. K., Jacobson, M. Z., Kaiser,  
30        J. W., Klimont, Z., Lohmann, U., Schwarz, J. P., Shindell, D., Storelvmo, T.,  
31        Warren, S. G., and Zender, C. S.: Bounding the role of black carbon in the climate  
32        system: A scientific assessment, *J. Geophys. Res.*, 118, 5380–5552, doi:  
33        10.1002/jgrd.50171, 2013.

34        Bond, T. C., Streets, D. G., Yarber, K. F., Nelson, S. M., Woo, J. H., and Klimont, Z.:  
35        A technology-based global inventory of black and organic carbon emissions from  
36        combustion, *J. Geophys. Res.-Atmos.*, 109, D14203, doi:10.1029/2003JD003697,  
37        2004.

38        Bousserez, N., Henze, K. D., Perkins, A., Bowman, W. K., Lee, M., Liu, J., Deng, F.,  
39        Jones, B. A. D: Improved analysis error covariance matrix for high-dimensional  
40        variational inversions: application to source estimation using a 3D atmospheric  
41        transport model, *Q.J.R. Meteorol. Soc.*, doi: 10.1002/qj.2495

42        Buchard, V., M. da Silva, A., R. Colarco, P., Darmenov, A., A. Randles, C.,  
43        Govindaraju, R., Torres, O., Campbell, J., and Spurr, R.: Using the OMI Aerosol  
44        Index and Absorption Aerosol Optical Depth to evaluate the NASA MERRA

1 Aerosol Reanalysis, *Atmos. Chem. Phys. Discuss.*, 14, 32177–32231,  
2 doi:10.5194/acpd-14-32177-2014, 2014.

3 Byrd, R. H., Lu, H. P., Nocedal, J., and Zhu, C. Y.: A limited memory algorithm for  
4 bound constrained optimization, *SIAM J. Sci. Comput.*, 16(5), 1190–1208, 1995

5 Cao, J. J., Lee, S. C., Chow, J. C., Watson, J. G., Ho, K. F., Zhang, R. J., Jin, Z. D.,  
6 Shen, Z. X., Chen, G. C., Kang, Y. M., Zou, S. C., Zhang, L. Z., Qi, S. H., Dai,  
7 M. H., Cheng, Y., and Hu, K.: Spatial and seasonal distributions of carbonaceous  
8 aerosols over China, *J. Geophys. Res.*, 112, D22S11, doi:10.1029/2006JD008205,  
9 2007.

10 Cao, J. J., Zhu, C. S., Chow, J. C., Watson, J. G., Han, Y. M., Wang, G., Shen, Z., and  
11 An, Z. S.: Black carbon relationships with emissions and meteorology in Xi'an,  
12 China, *Atmos. Res.*, 94, 194–202, 2009

13 Charlson, R. J., and Pilat, M. J.: Climate: The influence of aerosols, *J. Appl. Met.*,  
14 8(5), 1001–1002, 1969

15 Chen, D., Wang, Y., McElroy, M. B., He, K., Yantosca, R. M., and Le Sager, P.:  
16 Regional CO pollution and export in China simulated by the high-resolution  
17 nested-grid GEOS-Chem model, *Atmos. Chem. Phys.*, 9, 3825–3839,  
18 doi:10.5194/acp-9-3825-2009, 2009

19 Chin, M., Ginoux, P., Kinne, S., Torres, O., Holben, B. N., Duncan, B. N., Martin, R.  
20 V., Logan, J. A., Higurashi, A., and Nakajima, T.: Tropospheric aerosol optical  
21 thickness from the GOCART model and comparisons with satellite and sun  
22 photometer measurements, *J. Atmos. Sci.*, 59, 461–483, 2002.

23 Chow, J. C., Watson, G. J., Doraiswamy, P., Chen, W. A., L., Sodeman, A. D.,  
24 Lowenthal, H. D., Park, K., Arnott, P. W., and Motallebi, N.: Aerosol light  
25 absorption, black carbon, and elemental carbon at the Fresno Supersite,  
26 California, *Atmos. Res.*, 93(4), 874–887, 2009

27 Cohen, J. B. and Prinn, R. G.: Development of a fast, urban chemistry metamodel for  
28 inclusion in global models, *Atmos. Chem. Phys.*, 11, 7629–7656,  
29 doi:10.5194/acp-11-7629-2011, 2011.

30 Cohen, J. B., Prinn, R. G., and Wang, C.: The impact of detailed urban-scale  
31 processing on the composition, distribution, and radiative forcing of  
32 anthropogenic aerosols, *Geophys. Res. Lett.*, 38, L10808,  
33 doi:10.1029/2011GL047417, 2011.

34 Cohen, J. B. and Wang, C.: Estimating Global Black Carbon Emissions Using a Top-  
35 Down Kalman Filter Approach, *J. Geophys. Res. Atmos.*, 119, 307–  
36 323doi: 10.1002/2013JD019912, 2014.

37 Cohen, J. B.: Quantifying the occurrence and magnitude of the Southeast Asian fire,  
38 *Environ. Res. Lett.* 9, 114018 (13pp) 2014

39 Cooke, W. F., Liousse, C., Cachier, H., and Feichter, J.: Construction of a 1°x1° fossil  
40 fuel emission data set for carbonaceous aerosol and implementation and  
41 radiative impact in the ECHAM4 model, *J. Geophys. Res.*, 104, 22137–22162,  
42 1999.

43 Cozic, J., Verheggen, B., Mertes, S., Connolly, P., Bower, K., Petzold, A.,  
44 Baltensperger, U., and Weingartner, E.: Scavenging of black carbon in mixed

1 phase clouds at the high alpine site Jungfraujoch, *Atmos. Chem. Phys.*, 7, 1797–  
2 1807, 2007

3 Dana, M. T. and Hales, J. M.: Statistical aspects of washout of polydisperse aerosols,  
4 *Atmos. Environ.*, 10, 45–50, 1976

5 Dubovik, O. and King, D. M.: A flexible inversion algorithm for retrieval of aerosol  
6 optical properties from Sun and sky radiance measurements, *J. Geophys. Res.*,  
7 105, 20,673–20,696, 2000.

8 Dubovik, O., Holben, B. N., Eck, T. F., Smirnov, A., Kaufman, Y. J., King, M. D.,  
9 Tanré, D., and Slutsker, I.: Variability of absorption and optical properties of key  
10 aerosol types observed in worldwide locations, *J. Atmos. Sci.*, 59, 590–608,  
11 2002a.

12 Dubovik, O., Holben, B. N., Lapyonok, T., Sinyuk, A., Mishchenko, M. I., Yang P.,  
13 and Slutsker, I.: Non-spherical aerosol retrieval method employing light  
14 scattering by spheroids, *Geophys. Res. Lett.*, 29(10), 10.1029/2001GL014506,  
15 2002b.

16 Dubovik, O., Sinyuk, A., Lapyonok, T., Holben, B.N., Mishchenko, M., Yang, P., Eck,  
17 T.F., Volten, H., Muñoz, O., Veihelmann, B., van der Zande, W.J., Leon, J.-F.,  
18 Sorokin, M., and Slutsker, I.: Application of spheroid models to account for  
19 aerosol particle nonsphericity in remote sensing of desert dust. *J. Geophys. Res.*,  
20 111, D11208, doi:10.1029/2005JD006619, 2006.

21 Dubovik, O., Smirnov, A., Holben, B.N., King, M.D., Kaufman, Y. J., Eck, T.F., and  
22 Slutsker, I.: Accuracy assessment of aerosol optical properties retrieval from  
23 AERONET sun and sky radiance measurements, *J. Geophys. Res.*, 105, 9791–  
24 9806, 2000.

25 Eck, T. F., Holben, B. N., Reid, J. S., Dubovik, O., Smirnov, A., O'Neill, N. T.,  
26 Slutsker, I., and Kinne, S.: Wavelength dependence of the optical depth of  
27 biomass burning, urban, and desert dust aerosols, *J. Geophys. Res.*, 104(D24),  
28 31,333–31,349, 1999

29 Fairlie, T. D., Jacob, J. D., Dibb, E. J., Alexander, B., Avery, A. M., van Donkelaar, A.,  
30 and Zhang, L.: Impact of mineral dust on nitrate, sulfate, and ozone in  
31 transpacific Asian pollution plumes, *Atmos. Chem. Phys.*, 10, 3999–4012,  
32 doi:10.5194/acp-10-3999-2010, 2010.

33 Flanner, M. G., Zender, C. S., Randerson, J. T., and Rasch, P. J.: Present-day climate  
34 forcing and response from black carbon in snow, *Geophys. Res.-Atmos.*, 112,  
35 D11202, 10.1029/2006jd008003, 2007

36 Forster, P., Ramawamy, V., Artaxo, P., Bernsten, T., Betts, R., Fahey, D., Haywood, J.,  
37 Lean, J., Lowe, D., Myhre, G., Nganga, J., Prinn, R., Raga, G., Schulz, M., and  
38 Dorland, V. R.: Changes in Atmospheric Constituents and in Radiative Forcing,  
39 in: *Climate Change 2007: The Physical Science Basis. Contributions of working*  
40 *group I to the fourth Assessment Report on the Intergovernmental Panel on*  
41 *Climate Change*, edited by Solomon, S., Wuin, D., Manning, M., Chen, A.,  
42 Marquis, M., Averyt, K., Tignor, M., and Miller, H., Cambridge University  
43 Press, Cambridge, United Kingdom and New York, NY, USA, 2007

44 Fu, T.-M., Cao, J. J., Zhang, X. Y., Lee, S. C., Zhang, Q., Han, Y. M., Qu, W. J.,

1 Han, Z., Zhang, R., Wang, Y. X., Chen, D., and Henze, D. K.: Carbonaceous  
2 aerosols in China: top-down constraints on primary sources and estimation of  
3 secondary contribution, *Atmos. Chem. Phys.*, 12, 2725–2746, doi:10.5194/acp-  
4 12-2725-2012, 2012.

5 Giglio, L., Randerson, J. T., van der Werf, G. R., Kasibhatla, P. S., Collatz, G. J.,  
6 Morton, D. C., and DeFries, R. S.: Assessing variability and long-term trends in  
7 burned area by merging multiple satellite fire products, *Biogeosciences*, 7, 1171–  
8 1186, 2010.

9 Giglio, L., van der Werf, G. R., Randerson, J. T., Collatz, G. J., and Kasibhatla, P.:  
10 Global estimation of burned area using MODIS active fire observations, *Atmos.*  
11 *Chem. Phys.*, 6, 957–974, doi:10.5194/acp-6-957-2006, 2006.

12 Ginoux, P., Prospero, M. J., Torres, O., and Chin, M.: Long-term simulation of global  
13 dust distribution with the GOCART model: correlation with North Atlantic  
14 oscillation. *Environ. Modell. and Softw.*, 19, 113–128, 2004.

15 Hakami, A., Henze, K. D., Seinfeld, H. J., Chai, T., Tang, Y., Carmichael, R. G., and  
16 Sandu, A.: Adjoint inverse modeling of black carbon during the Asian Pacific  
17 Regional Aerosol Characterization Experiment, *J. Geophys. Res.*, 110, D14301,  
18 doi:10.1029/2004JD005671, 2005.

19 Hansen, A. D. A., Rosen, H., and Novakov, T.: The Aethalometer—An Instrument for  
20 the Real-Time Measurement of Optical Absorption by Aerosol Particles, *Sci.*  
21 *Total Environ.* 36:191–196, 1984.

22 Hansen, J., Sato, M., Ruedy, R., Lacis, A., and Oinas, V.: Global warming in the  
23 twenty-first century: An alternative scenario, *P. Natl. Acad. Sci. USA*, 97(18),  
24 9875–9880, 2000.

25 Hansen, J., and Nazarenko, L.: Soot climate forcing via snow and ice albedos, *Proc.*  
26 *Natl. Acad. Sci.* 101(2), 423–428, doi:10.1073/pnas.2237157100, 2004. Hansen,  
27 J., Sato, M., Ruedy, R., Nazarenko, L., Lacis, A., Schmidt, G. A., Russell, G.,  
28 Aleinov, I., Bauer, M., Bauer, S., Bell, N., Cairns, B., Canuto, V., Chandler, M.,  
29 Cheng, Y., Del Genio, A., Faluvegi, G., Fleming, E., Friend, A., Hall, T.,  
30 Jackman, C., Kelley, M., Kiang, N., Koch, D., Lean, J., Lerner, J., Lo, K.,  
31 Menon, S., Miller, R., Minnis, P., Novakov, T., Oinas, V., Perlwitz, Ja., Perlwitz,  
32 Ju., Rind, D., Romanou, A., Shindell, D., Stone, P., Sun, S., Tausnev, N.,  
33 Thresher, D., Wielicki, B., Wong, T., Yao, M., and Zhang, S.: Efficacy of climate  
34 forcings, *J. Geophys. Res.*, 110, D18104, doi: 10.1029/2005JD005776, 2005.

35 Hansen, P. C.: Rank-Deficient and Discrete Ill-Posed Problems: Numerical Aspects of  
36 Linear Inversion, SIAM, Philadelphia, USA, 1998.

37 Heald, C. L., Jacob, J. D., Park, J. R., Russell, M. L., Huebert, J. B., Seinfeld, H. J.,  
38 Liao, H., and Weber, J. R.: A large organic aerosol source in the free  
39 troposphere missing from current models, *Geophys. Res. Lett.*, 32, L18809,  
40 doi:10.1029/2005GL023831, 2005.

41 Henze, D. K., Hakami, A., and Seinfeld, H. J.: Development of the adjoint of GEOS-  
42 Chem, *Atmos. Chem. Phys.*, 7, 2413–2433, 2007.

43 Henze, D. K., Seinfeld, J. H., and Shindell, D. T.: Inverse modeling and mapping US  
44 air quality influences of inorganic PM<sub>2.5</sub> precursor emissions using the adjoint

1 of GEOS-Chem, *Atmos. Chem. Phys.*, 9, 5877–5903, doi: 10.5194/acp-9-5877-  
2 2009, 2009.

3 Hoffer, A., Gelencser, A., Guyon, Kiss, P., G., Schmid, O., Frank, P. G., Artaxo, P.,  
4 and Andreae, O. M.: Optical properties of humic-like substances (HULIS) in  
5 biomass-burning aerosols, *Atmos. Chem. Phys.*, 6, 3563–3570, 2006.

6 Holben, B. N., Eck, F. T., Slutsker, I., Tanré, D., Buis, P. J., Setzer, A., Vermote, E.,  
7 Reagan, A. J., Kaufman, J. Y., Nakajima, T., Lavenu, F., Jankowiak, I., Smirnov,  
8 A.: AERONET--A federated instrument network and data archive for aerosol  
9 characterization, *Remote Sens. Environ.*, 66, 1–16, 1998.

10 Hu, Y., Napelenok, L. S., Odman, T. M., and Russell, G. A.: Sensitivity of inverse  
11 estimation of 2004 elemental carbon emissions inventory in the United States to  
12 the choice of observational networks, *Geophys. Res. Lett.*, 36, L15806,  
13 doi:10.1029/2009GL039655, 2009a

14 Hu, Y., Odman, T. M., and Russell, G. A., Top-down analysis of the elemental carbon  
15 emissions inventory in the United States by inverse modeling using Community  
16 Multiscale Air Quality model with decoupled direct method (CMAQ-DDM), *J.*  
17 *Geophys. Res.*, 114, D24302, doi:10.1029/2009JD011987, 2009b

18 Huneus, N., Boucher, O., and Chevallier, F.: Atmospheric inversion of SO<sub>2</sub> and  
19 primary aerosol emissions for the year 2010, *Atmos. Chem. Phys.*, 13, 6555-  
20 6573, doi:10.5194/acp-13-6555-2013, 2013.

21 Jacobson, M. Z.: A physically-based treatment of elemental carbon optics:  
22 Implications for global direct forcing of aerosols, *Geophys. Res. Lett.*, 27(2),  
23 217–220, doi:10.1029/1999GL010968, 2000.

24 Jacobson, M. Z.: Isolating nitrated and aromatic aerosols and nitrated aromatic gases  
25 as sources of ultraviolet light absorption, *J. Geophys. Res.-Atmos.*, 104(D3),  
26 3527–3542, 1999

27 Janssen N.A., Hoek G., Simic-Lawson M., Fischer P., van Bree L., ten Brink H.,  
28 Keuken, M; Atkinson, R. W., Anderson, H. R., Brunekreef, B., Cassee, F. R.:  
29 Black Carbon as an Additional Indicator of the Adverse Health Effects of  
30 Airborne Particles Compared with PM<sub>10</sub> and PM<sub>2.5</sub>. *Environ Health Perspect*  
31 119:1691–1699, 2011.

32 Janssen NAH, Lanki, T., Hoek, G., Vallius, M., de Hartog, J. J., Van Grieken, R.,  
33 Pekkanen, J., Brunekreef, B.: Associations between ambient, personal and  
34 indoor exposure to fine particulate matter constituents in Dutch and Finnish  
35 panels of cardiovascular patients. *Occup. Environ. Med.*, 62:868–877, 2005

36 Jethva, H. and Torres, O.: Satellite-based evidence of wavelengthdependent aerosol  
37 absorption in biomass burning smoke inferred from Ozone Monitoring  
38 Instrument, *Atmos. Chem. Phys.*, 11, 10541–10551, doi:10.5194/acp-11-10541-  
39 2011, 2011.

40 Jethva, H., Torres, O., and Ahn, C.: Global assessment of OMI aerosol single-  
41 scattering albedo using ground-based AERONET inversion, *J. Geophys. Res.*  
42 *Atmos.*, 119, 9020–9040, doi:10.1002/2014JD021672, 2014.

43 Jiang, Z., Jones, B. A. D., Kopacz, M., Liu, J., Henze, K., D., and Heald, C.:  
44 Quantifying the impact of model errors on top-down estimates of carbon

1 monoxide emissions using satellite observations, *J. Geophys. Res.*, 116,  
2 D15306, doi:10.1029/2010JD015282, 2011.

3 Johnson, B. T., Shine, P. K., and Forster, M. P.: The semi-direct aerosol effect: Impact  
4 of absorbing aerosols on marine stratocumulus, *Quart J. Roy. Meteor. Soc.*,  
5 130(599), 1407–1422, doi:10.1256/qj.03.61, 2004.

6 Kirchstetter, T. W., Novakov, T., and Hobbs, V. P.: Evidence that the spectral  
7 dependence of light absorption by aerosols is affected by organic carbon, *J.*  
8 *Geophys. Res.-Atmos.*, 109, D21208, doi:10.1029/2004JD004999.12, 2004.

9 Koch, D., Schulz, M., Kinne, S., McNaughton, C., Spackman, J. R., Balkanski, Y.,  
10 Bauer, S., Bernsten, T., Bond, T. C., Boucher, O., Chin, M., Clarke, A.,  
11 De Luca, N., Dentener, F., Diehl, T., Dubovik, O., Easter, R., Fahey, D. W.,  
12 Feichter, J., Fillmore, D., Freitag, S., Ghan, S., Ginoux, P., Gong, S.,  
13 Horowitz, L., Iversen, T., Kirkevåg, A., Klimont, Z., Kondo, Y., Krol, M.,  
14 Liu, X., Miller, R., Montanaro, V., Moteki, N., Myhre, G., Penner, J. E.,  
15 Perlwitz, J., Pitari, G., Reddy, S., Sahu, L., Sakamoto, H., Schuster, G.,  
16 Schwarz, J. P., Seland, Ø., Stier, P., Takegawa, N., Takemura, T., Textor, C.,  
17 van Aardenne, J. A., and Zhao, Y.: Evaluation of black carbon estimations in  
18 global aerosol models, *Atmos. Chem. Phys.*, 9, 9001-9026, doi:10.5194/acp-9-  
19 9001-2009, 2009.

20 Kok, J. F.: A scaling theory for the size distribution of emitted dust aerosols suggests  
21 climate models underestimate the size of the global dust cycle, *P. Natl. Acad.*  
22 *Sci.*, 108(3), 1016-1021, 2011

23 Kondo, Y., Oshima, N., Kajino, M., Mikami, R., Moteki, N., Takegawa, N., Verma, L.  
24 R., Kajii, Y., Kato, S., and Takami, A.: Emissions of black carbon in East Asia  
25 estimated from observations at a remote site in the East China Sea, *J. Geophys.*  
26 *Res.*, 116, D16201, doi:10.1029/2011JD015637, 2011

27 Kopacz, M., Jacob, D. J., Fisher, J. A., Logan, J. A., Zhang, L., Megretskaya, I. A.,  
28 Yantosca, R. M., Singh, K., Henze, D. K., Burrows, J. P., Buchwitz, M.,  
29 Khlystova, I., McMillan, W. W., Gille, J. C., Edwards, D. P., Eldering, A.,  
30 Thouret, V., and Nedelec, P.: Global estimates of CO sources with high  
31 resolution by adjoint inversion of multiple satellite datasets (MOPITT, AIRS,  
32 SCIAMACHY, TES), *Atmos. Chem. Phys.*, 10, 855-876, doi:10.5194/acp-10-  
33 855-2010, 2010.

34 Kopacz, M., Jacob, J. D., Henze, K. D., Heald, L. C., Streets, G. D., and Zhang, Q.: A  
35 comparison of analytical and adjoint Bayesian inversion methods for  
36 constraining Asian sources of CO using satellite (MOPITT) measurements of  
37 CO columns, *J. Geophys. Res.*, 114, D04305, doi:10.1029/2007JD009264,  
38 2009.

39 Kopacz, M., Mauzerall, D. L., Wang, J., Leibensperger, E. M., Henze, D. K., and  
40 Singh, K.: Origin and radiative forcing of black carbon transported to the  
41 Himalayas and Tibetan Plateau, *Atmos. Chem. Phys.*, 11, 2837-2852,  
42 doi:10.5194/acp-11-2837-2011, 2011.

43 Krol, M., Houweling, S., Bregman, B., van den Broek, M., Segers, A.,  
44 van Velthoven, P., Peters, W., Dentener, F., and Bergamaschi, P.: The two-way

1        nested global chemistry-transport zoom model TM5: algorithm and applications,  
2        *Atmos. Chem. Phys.*, 5, 417–432, doi:10.5194/acp-5-417-2005, 2005.

3        Ku, B., and Park, J. R.: Inverse modeling analysis of soil dust sources over East Asia,  
4        *Atmos. Environ.*, 45(32), 5903–5912, doi:10.1016/j.atmosenv.2011.06.078,  
5        2011

6        Levelt, P. F., Hilsenrath, E., Leppelmeier, G. W., van den Oord, G. H. J., Bhartia, P.  
7        K., Tamminen, J., de Haan, J. F., Veefkind, J. P.: Science objectives of the  
8        Ozone Monitoring Instrument, *IEEE Trans. Geosci. Remote Sens.*, 44(5), 1199–  
9        1208, doi:10.1109/TGRS.2006.872336, 2006b.

10       Levelt, P. F., van den Oord, G. H. J., Dobber, M. R., Mälkki, A., Visser, H., de Vries,  
11       J., Stammes, P., Lundell, J. O. V., Saari, H.: The Ozone Monitoring Instrument,  
12       *IEEE Trans. Geosci. Remote Sens.*, 44(5), 1093–1101,  
13       doi:10.1109/TGRS.2006.872333, 2006a.

14       Lions, J. L.: *Optimal Control of Systems Governed by Partial Differential Equations*;  
15       Springer-Verlag: Berlin, 1971.

16       Liu, H. Y., Jacob, J. D., Bey, I., and Yantosca, M. R.: Constraints from Pb-210 and Be-  
17       7 on wet deposition and transport in a global three-dimensional chemical tracer  
18       model driven by assimilated meteorological fields, *J. Geophys. Res. Atmos.*,  
19       106, 12109–12128, 2001.

20       Liu, X. H., Penner, E. J., and Wang M. H.: Influence of anthropogenic sulfate and  
21       black carbon on upper tropospheric clouds in the NCAR CAM3 model coupled  
22       to the IMPACT global aerosol model, *J. Geophys. Res.*, 114, D03204,  
23       doi:10.1029/2008JD010492, 2009.

24       Lu, Z., Zhang, Q., and Streets, D. G.: Sulfur dioxide and primary carbonaceous  
25       aerosol emissions in China and India, 1996–2010, *Atmos. Chem. Phys.*, 11,  
26       9839–9864, doi:10.5194/acp-11-9839-2011, 2011.

27       Luo, M., Rinsland, C. P., Logan, J. A., Worden, J., Kulawik, S., Eldering, A.,  
28       Goldman, A., Shephard, M. W., Gunson, M., Lampel M.: Comparison of carbon  
29       monoxide measurements by TES and MOPITT: The influence of a priori data  
30       and instrument characteristics on nadir atmospheric species retrievals, *J.*  
31       *Geophys. Res.*, 112, D09303, doi:10.1029/2006JD007663, 2007.

32       Ma, X., Yu, F., and Luo, G.: Aerosol direct radiative forcing based on GEOS-Chem-  
33       APM and uncertainties, *Atmos. Chem. Phys.*, 12, 5563–5581, doi:10.5194/acp-  
34       12-5563-2012, 2012.

35       Magi, B. I., Ginoux, P., Ming, Y., and Ramaswamy, V.: Evaluation of tropical and  
36       extratropical Southern Hemisphere African aerosol properties simulated by a  
37       climate model, *J. Geophys. Res.-Atmos.*, 114, D14204,  
38       doi:10.1029/2008JD011128, 2009.

39       Martin, R. V., Jacob, D. J., Yantosca, R. M., Chin, M., and Ginoux, P.: Global and  
40       regional decreases in tropospheric oxidants from photochemical effects of  
41       aerosols, *J. Geophys. Res.*, 108, 4097, doi:10.1029/2002JD002622, 2003.

42       Moorthy, K. K., Beegum, S. N., Srivastava, N., Satheesh, S.K., Chin, M., Blond, N.,  
43       Babu, S. S., Singh, S.: Performance evaluation of chemistry transport models  
44       over India, *Atmos. Environ.*, 71, 210–225, 2013.

1 Omar, A. H., Winker, D. M., Tackett, J. L., Giles, D. M., Kar, J., Liu, Z., Vaughan, M.  
2 A., Powell, K. A., and Trepte, C. R.: CALIOP and AERONET aerosol optical  
3 depth comparisons: One size fits none, *J. Geophys. Res. Atmos.*, 118, 4748–  
4 4766, doi:10.1002/jgrd.50330, 2013.

5 Oshima, N., Koike, M., Zhang, Y., Kondo, Y., Moteki, N., Takegawa, N., and  
6 Miyazaki, Y.: Aging of black carbon in outflow from anthropo-genic sources  
7 using a mixing state resolved model: Model development and evaluation, *J.*  
8 *Geophys. Res.*, 114, D06210, doi:10.1029/2008JD010680, 2009.

9 Park, R. J., Jacob, J. D., Chin, M., and Martin, R. V.: Sources of carbonaceous  
10 aerosols over the United States and implications for natural visibility, *J. Geophys.*  
11 *Res.*, 108(D12), 4355, doi:10.1029/2002JD003190, 2003

12 Philip, S., Martin, R. V., van Donkelaar, A., J., Lo, Wai-Ho, J., Wang, Y., Chen, D.,  
13 Zhang, L., Kasibhatla, P. S., Wang, S. W., Zhang, Q., Lu, Z., Streets, G. D.,  
14 Bittman, S., and Macdonald, J. D.: Global Chemical Composition of Ambient  
15 Fine Particulate Matter for Exposure Assessment, *Environ. Sci. Technol.*, 48(22),  
16 pp. 13060-13068. doi : 10.1021/es502965b, 2014

17 Pungler, E. M. and West, J. J.: The effect of grid resolution on estimates of the burden  
18 of ozone and fine particulate matter on premature mortality in the USA, *Air Qual.*  
19 *Atmos. Health*, 6, 563–573, doi:10.1007/s11869-013-0197-8, 2013.

20 Qian, Y., Gustafson, W. I., Leung, L. R., and Ghan, S. J.: Effects of soot-induced snow  
21 albedo change on snowpack and hydrological cycle in western United States  
22 based on Weather Research and Forecasting chemistry and regional climate  
23 simulations, *J. Geophys. Res.*, 114, D03108, doi:10.1029/2008JD011039, 2009

24 Ramanathan, V. and Carmichael, G.: Global and regional climate changes due to  
25 black carbon, *Nature Geoscience*, 1, 221-227, 2008.

26 Randerson, J. T., Liu, H., Flanner, M. G., Chambers, S. D., Jin, Y., Hess, P. G., Pfister,  
27 G., Mack, M. C., Treseder, K. K., Welp, L. R., Chapin, F. S., Harden, J. W.,  
28 Goulden, M. L., Lyons, E., Neff, J. C., Schuur, E., Zender, C. S.: The impact of  
29 boreal forest fire on climate warming, *Science*, 314, 1130-1132, 2006.

30 Ridley, D. A., Heald, L. C., and Ford, B.: North African dust export and deposition: A  
31 satellite and model perspective, *J. Geophys. Res.*, 117, D02202,  
32 doi:10.1029/2011JD016794, 2012.

33 Rodgers, C. D.: Inverse methods for atmospheric sounding, Series on Atmospheric,  
34 Oceanic and Planetary Physics, vol. 2, World Scientific, Singapore, 2000.

35 Satheesh, S. K., Torres, O., Remer, L. A., Babu, S. S., Vinoj, V., Eck, T. F., Kleidman,  
36 R. G., and Holben, B. N.: Improved assessment of aerosol absorption using  
37 OMI-MODIS joint retrieval, *J. Geophys. Res.*, 114, D05209,  
38 doi:10.1029/2008JD011024, 2009.

39 Satheesh, S. K., and Ramanathan, V.: Large differences in tropical aerosol forcing at  
40 the top of the atmosphere and Earth's surface, *Nature*, 405, 60–63,  
41 doi:10.1038/35011039, 2000

42 Schwartz, J., Coull, B., Laden, F., Ryan, L.: The effect of dose and timing of dose on  
43 the association between airborne particles and survival. *Environ Health*  
44 *Perspect* 116:64–69, 2008



1 Shen, Z., Liu, J., Horowitz, L. W., Henze, D. K., Fan, S., H., Levy II,  
2 Mauzerall, D. L., Lin, J.-T., and Tao, S.: Analysis of transpacific transport of  
3 black carbon during HIPPO-3: implications for black carbon aging, *Atmos.*  
4 *Chem. Phys.*, 14, 6315-6327, doi:10.5194/acp-14-6315-2014, 2014.

5 Silva, A. R., West, J. J., Zhang, Y., Aneberg, C. S., Lamarque, J.-F., Shindell, T. D.,  
6 Collins, J. W., Dalsoren, S., Faluvegl, G., Folbeth, G., Horowitz, W. L.,  
7 Nagashima, T., Nalk, V., Rumbold, S., Skele, R., Sudo, K., Takemura, T.,  
8 Bergmann, D., Camero-smith, P., Cionnl, I., Doherty, M. R., Eyring, V., Josse,  
9 B., MacKenzie, I. A., Plummer, D., Righl, M., Stevenson, S. D., Strode, S.,  
10 Szopa, S., Zeng, G.: Global premature mortality due to anthropogenic outdoor  
11 air pollution and the contribution of past climate change. *Environ. Res. Lett.* 8,  
12 034005 doi:10.1088/1748-9326/8/3/034005, 2013.

13 Sinyuk, A., Dubovik, O., Holben, B., Eck, T. F., Breon, F. M., Martonchik, J., Kahn,  
14 R., Diner, D. J., Vermote, E. F., Roger, J. C., Lapyonok, T., Slutsker, I.:  
15 Simultaneous retrieval of aerosol and surface properties from a combination of  
16 AERONET and satellite data. *Remote Sens. Environ.*, 107(2-Jan), 90-108, 2007.

17 Stier, P., Seinfeld, J. H., Kinne, S., Feichter, J., and Boucher, O.: Impact of  
18 nonabsorbing anthropogenic aerosols on clear-sky atmospheric absorption, *J.*  
19 *Geophys. Res.*, 111, D18201, doi:10.1029/2006JD007147, 2006.

20 Textor, C., Schulz, M., Guibert, S., Kinne, S., Balkanski, Y., Bauer, S., Bernsten, T.,  
21 Berglen, T., Boucher, O., Chin, M., Dentener, F., Diehl, T., Feichter, J.,  
22 Fillmore, D., Ginoux, P., Gong, S., Grini, A., Hendricks, J., Horowitz, L.,  
23 Huang, P., Isaksen, I. S. A., Iversen, T., Kloster, S., Koch, D., Kirkevåg, A.,  
24 Kristjansson, J. E., Krol, M., Lauer, A., Lamarque, J. F., Liu, X., Montanaro, V.,  
25 Myhre, G., Penner, J. E., Pitari, G., Reddy, M. S., Seland, Ø., Stier, P.,  
26 Takemura, T., and Tie, X.: The effect of harmonized emissions on aerosol  
27 properties in global models – an AeroCom experiment, *Atmos. Chem. Phys.*, 7,  
28 4489-4501, doi:10.5194/acp-7-4489-2007, 2007.

29 Torres, O., Ahn, C., and Chen, Z.: Improvements to the OMI near-UV aerosol  
30 algorithm using A-train CALIOP and AIRS observations, *Atmos. Meas. Tech.*,  
31 6, 3257-3270, doi:10.5194/amt-6-3257-2013, 2013.

32 Torres, O., Bhartia, P. K., Herman, J. R., and Ahmad, Z.: Derivation of aerosol  
33 properties from satellite measurements of backscattered ultraviolet radiation.  
34 Theoretical Basis, *J. Geophys. Res.*, 103(D14), 17,099– 17,110,  
35 doi:10.1029/98JD00900, 1998.

36 Torres, O., Bhartia, P. K., Sinyuk, A., Welton, E. J., and Holben, B.: Total Ozone  
37 Mapping Spectrometer measurements of aerosol absorption from space:  
38 Comparison to SAFARI 2000 ground-based observations, *J. Geophys. Res.*,  
39 110, D10S18, doi:10.1029/2004JD004611, 2005.

40 Torres, O., Tanskanen, A., Veihelmann, B., Ahn, C., Braak, R., Bhartia, P. K.,  
41 Veefkind, P., and Levelt P.: Aerosols and surface UV products from Ozone  
42 Monitoring Instrument observations: An overview, *J. Geophys. Res.*, 112,  
43 D24S47, doi:10.1029/2007JD008809, 2007.

44 United Nations Environment Program and World Meteorological Organization,

1 “Integrated Assessment of Black Carbon and Tropospheric Ozone” (Nairobi,  
2 2011).

3 van der Werf, G. R., Randerson, J. T., Giglio, L., Collatz, G. J., Kasibhatla, P. S., and  
4 Arellano Jr., A. F.: Interannual variability in global biomass burning emissions  
5 from 1997 to 2004, *Atmos. Chem. Phys.*, 6, 3423-3441, doi:10.5194/acp-6-  
6 3423-2006, 2006.

7 van der Werf, G. R., Randerson, J. T., Giglio, L., Collatz, G. J., Mu, M., Kasibhatla, P.  
8 S., Morton, D. C., DeFries, R. S., Jin, Y., and van Leeuwen, T. T.: Global fire  
9 emissions and the contribution of deforestation, savanna, forest, agricultural,  
10 and peat fires (1997–2009), *Atmos. Chem. Phys.*, 10, 11707–11735, doi:  
11 10.5194/acp-10-11707-2010, 2010.

12 van Donkelaar, A., Martin, R. V., Spurr, R. J. D., Drury, E., Remer, L. A., Levy, R.  
13 C., and Wang, J.: Optimal estimation for global ground-level fine particulate  
14 matter concentrations, *J. Geophys. Res. Atmos.*, 118, 5621–5636,  
15 doi:10.1002/jgrd.50479, 2013

16 Wang, J., Xu, X., Henze, K. D., Zeng, J., Ji, Q., Tsay, S.-C., and Huang, J.: Top-down  
17 estimate of dust emissions through integration of MODIS and MISR aerosol  
18 retrievals with the GEOS-Chem adjoint model, *Geophys. Res. Lett.*, 39,  
19 L08802, doi:10.1029/2012GL051136, 2012.

20 Wang, Q., Jacob, D. J., Fisher, J. A., Mao, J., Leibensperger, E. M., Carouge, C. C.,  
21 Le Sager, P., Kondo, Y., Jimenez, J. L., Cubison, M. J., and Doherty, S. J.:  
22 Sources of carbonaceous aerosols and deposited black carbon in the Arctic in  
23 winter-spring: implications for radiative forcing, *Atmos. Chem. Phys.*, 11,  
24 12453-12473, doi:10.5194/acp-11-12453-2011, 2011.

25 Wang, X., Wang, Y., Hao, J., Kondo, Y., Irwin, M., Munger, J. W., and Zhao, Y.: Top-  
26 down estimate of China’s black carbon emissions using surface observations:  
27 Sensitivity to observation representativeness and transport model error, *J.*  
28 *Geophys. Res. Atmos.*, 118, 5781–5795, doi:10.1002/jgrd.50397, 2013.

29 Wang, Y. X., McElroy, B. M., Jacob, J. D., and Yantosca, R. M.: A nested grid  
30 formulation for chemical transport over Asia: Applications to CO, *J. Geophys.*  
31 *Res.*, 109, D22307, doi:10.1029/2004JD005237, 2004.

32 Wang, Y., Jacob, J. D., and Logan, A. J.: Global simulation of tropospheric O<sub>3</sub>-NO<sub>x</sub>-  
33 hydrocarbon chemistry, 1. Model formulation, *J. Geophys. Res.*, 103/D9,  
34 10,713-10,726, 1998.

35 Wecht, K. J., J. D., Jacob, Wofsy, C. S., Kort, A. E., Worden, R. J., Kulawik, S. S.,  
36 Henze, K. D., Kopacz, M., and Payne, H. V.: Validation of TES methane with  
37 HIPPO aircraft observations: implications for inverse modeling of methane  
38 sources, *Atmos. Chem. Phys.*, 12, 1823-1832, 2012.

39 Wecht, K. J., Jacob, J. D., Frankenberg, C., Jiang, Z., and Blake, D. R.: Mapping of  
40 North American methane emissions with high spatial resolution by inversion of  
41 SCIAMACHY satellite data, *J. Geophys. Res. Atmos.*, 119, 7741–7756  
42 doi:10.1002/2014JD021551, 2014

43 Wesely, M. L.: Parameterization of surface resistance to gaseous dry deposition in  
44 regional-scale numerical models, *Atmos. Environ.*, 23, 1293-1304, 1989.

1 Worden, H. M., Logan, J. A., Worden, J. R., Beer, R., Bowman, K., Clough, S. A.,  
2 Eldering, A., Fisher, B. M., Gunson, M. R., Herman, R. L., Kulawik, S. S.,  
3 Lampel, M. C., Luo, M., Meqretskaya, I. A., Osterman, G. B., Shephard, M. W.:  
4 Comparisons of Tropospheric Emission Spectrometer (TES) ozone profiles to  
5 ozonesondes: Methods and initial results, *J. Geophys. Res.*, 112, D03309,  
6 doi:10.1029/2006JD007258, 2007.

7 Xu, X., Wang, J., Henze, K. D., Qu, W., Kopacz, M.: Constraints on Aerosol Sources  
8 Using GEOS-Chem Adjoint and MODIS Radiances, and Evaluation with Multi-  
9 sensor (OMI, MISR) data, *J. Geophys. Res.*, 118, 6396–6413  
10 doi:10.1002/jgrd.50515, 2013

11 Zhang L., Liao, H., Li, J.: Impacts of Asian Summer Monsoon on Seasonal and  
12 Interannual Variations of Aerosols over Eastern China. *J. Geophys. Res.*, 115,  
13 D00K05, doi:10.1029/2009JD012299, 2010.

14 Zhang, L., Jacob, J. D., Kopacz, M., Henze, K. D., Singh, K., and Jaffe, D. A.:  
15 Intercontinental source attribution of ozone pollution at western U.S. sites using  
16 an adjoint method, *Geophys. Res. Lett.*, 36, L11810,  
17 doi:10.1029/2009GL037950, 2009.

18 Zhang, L., Kok, J., Henze, K. D., Li, Q. B., and Zhao, C.: Improving simulations of  
19 fine dust surface concentrations over the Western United States by optimizing  
20 the particle size distribution, *Geophys. Res. Lett.*, 40, 3270–3275, doi:  
21 10.1002/grl.50591, 2013.

22 Zhang, Q., Streets, D. G., Carmichael, G. R., He, K. B., Huo, H., Kannari, A.,  
23 Klimont, Z., Park, I. S., Reddy, S., Fu, J. S., Chen, D., Duan, L., Lei, Y., Wang,  
24 L. T., and Yao, Z. L.: Asian emissions in 2006 for the NASA INTEX-B mission,  
25 *Atmos. Chem. Phys.*, 9, 5131–5153, 2009.

26 Zhang, X. Y., Wang, Y. Q., Zhang, X. C., Guo, W., Gong, S. L., Zhao, P., and Jin, J.  
27 L.: Carbonaceous aerosol composition over various regions of China during  
28 2006, *J. Geophys. Res.*, 113, D14111, doi:10.1029/2007JD009525, 2008

29 Zhao, C., Liu, X., Leung, L. R., Johnson, B., McFarlane, S. A., Gustafson Jr., W. I.,  
30 Fast, J. D., and Easter, R.: The spatial distribution of mineral dust and its  
31 shortwave radiative forcing over North Africa: modeling sensitivities to dust  
32 emissions and aerosol size treatments, *Atmos. Chem. Phys.*, 10, 8821–8838,  
33 doi:10.5194/acp-10-8821-2010, 2010.

34 Zhu, C., Byrd, R. H., Lu, P., and Nocedal, J.: L-BFGS-B: A limited memory  
35 FORTRAN code for solving bound constrained optimization problems, Tech.  
36 Rep., Northwestern University, 1994

37 Zhu, L., Henze, K. D., Cady-Pereira, K. E., Shephard, M. W., Luo, M., Pinder, R. W.,  
38 Bash, J. O., Jeong, G.: Constraining U.S. ammonia emissions using TES remote  
39 sensing observations and the GEOS-Chem adjoint model, *J. Geophys. Res.*, 118,  
40 3355–3368, doi:10.1002/jgrd.50166, 2013.

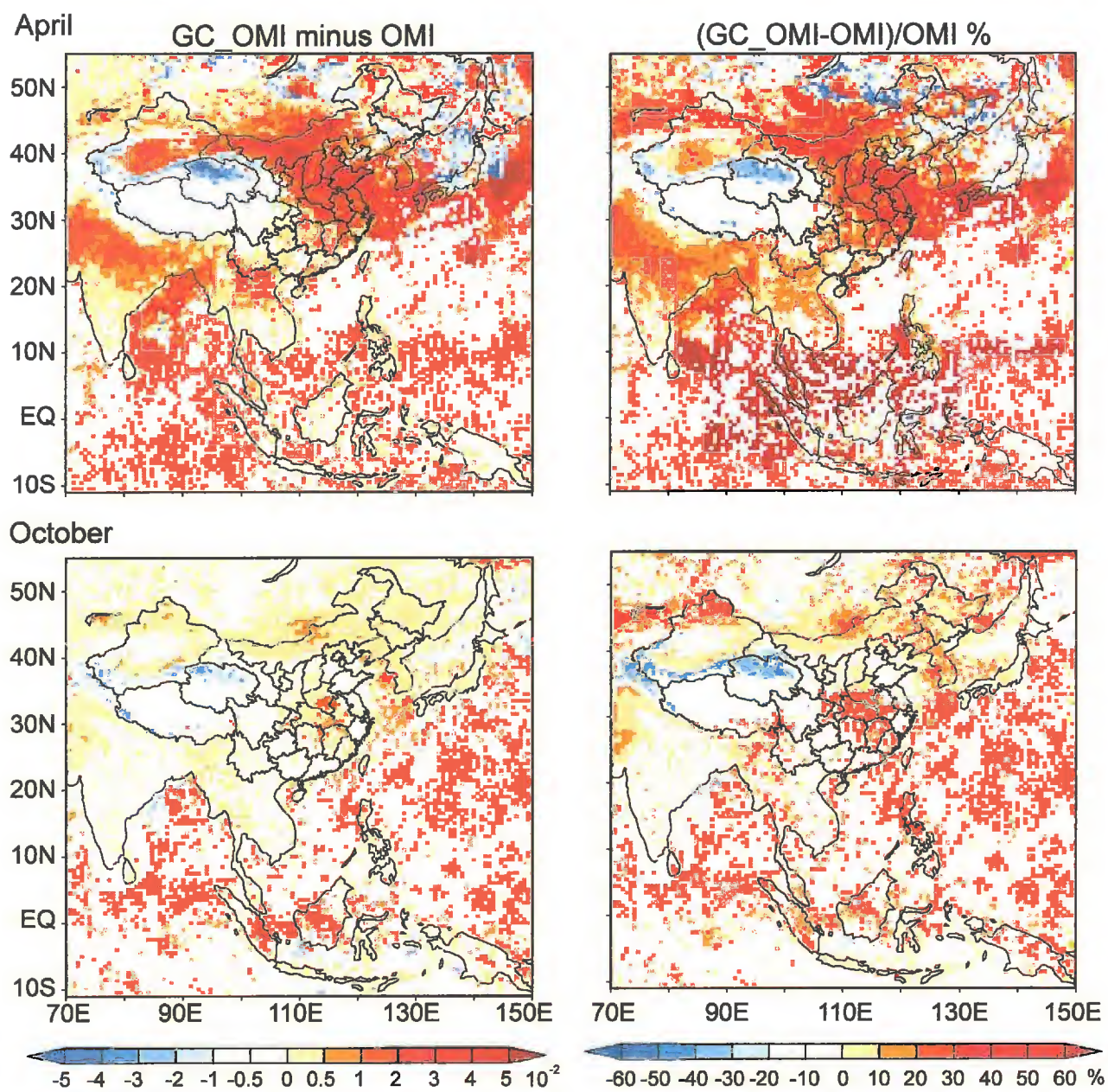


Fig. 1



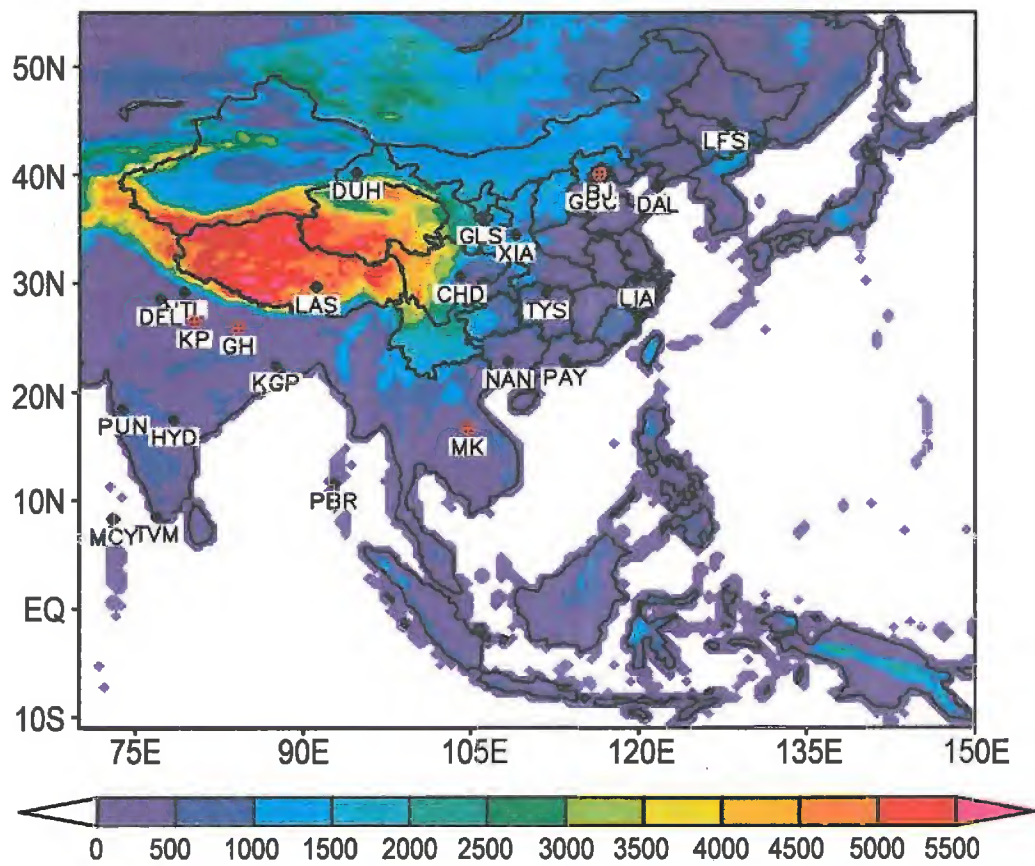


Fig. 2

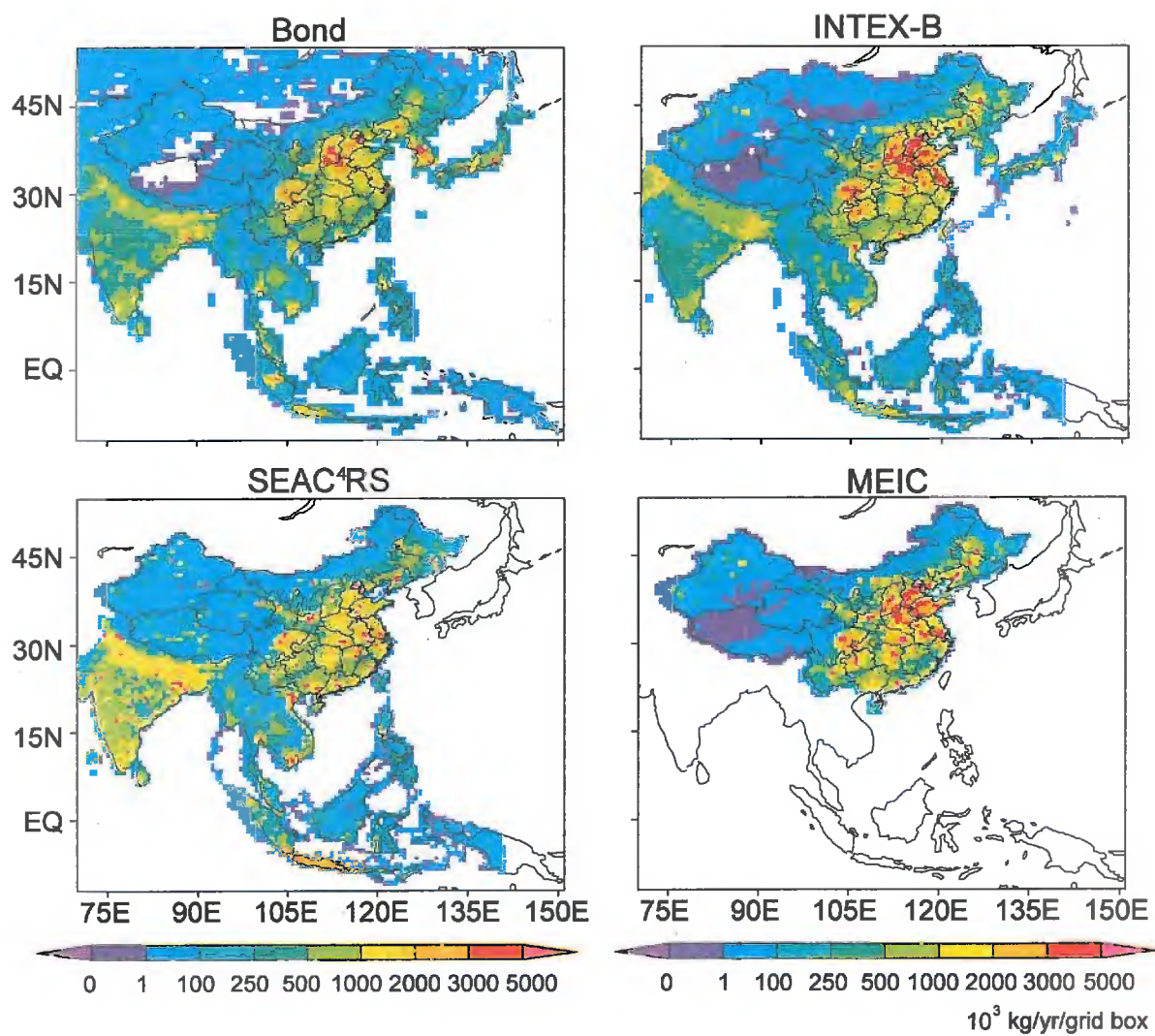


Fig. 3

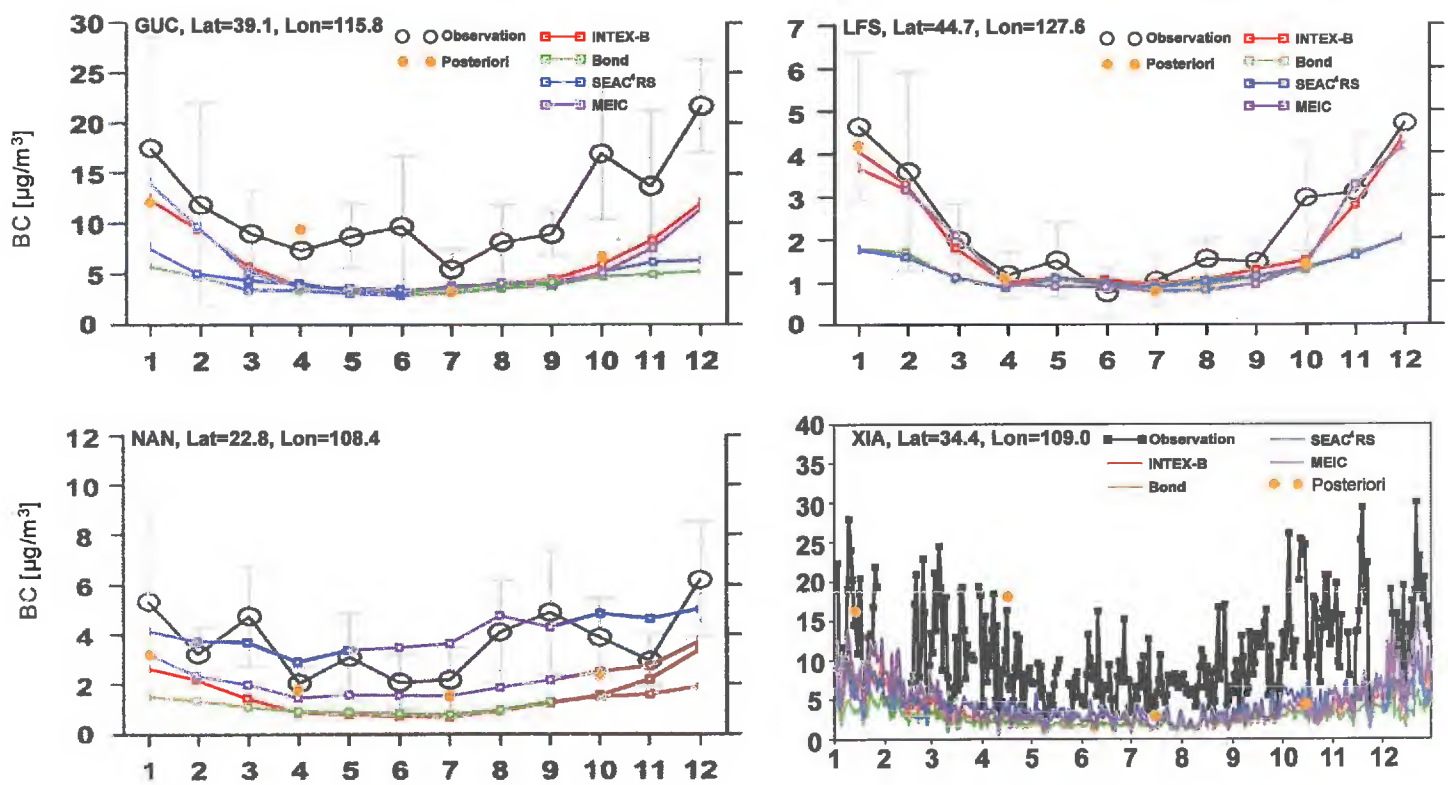


Fig. 4



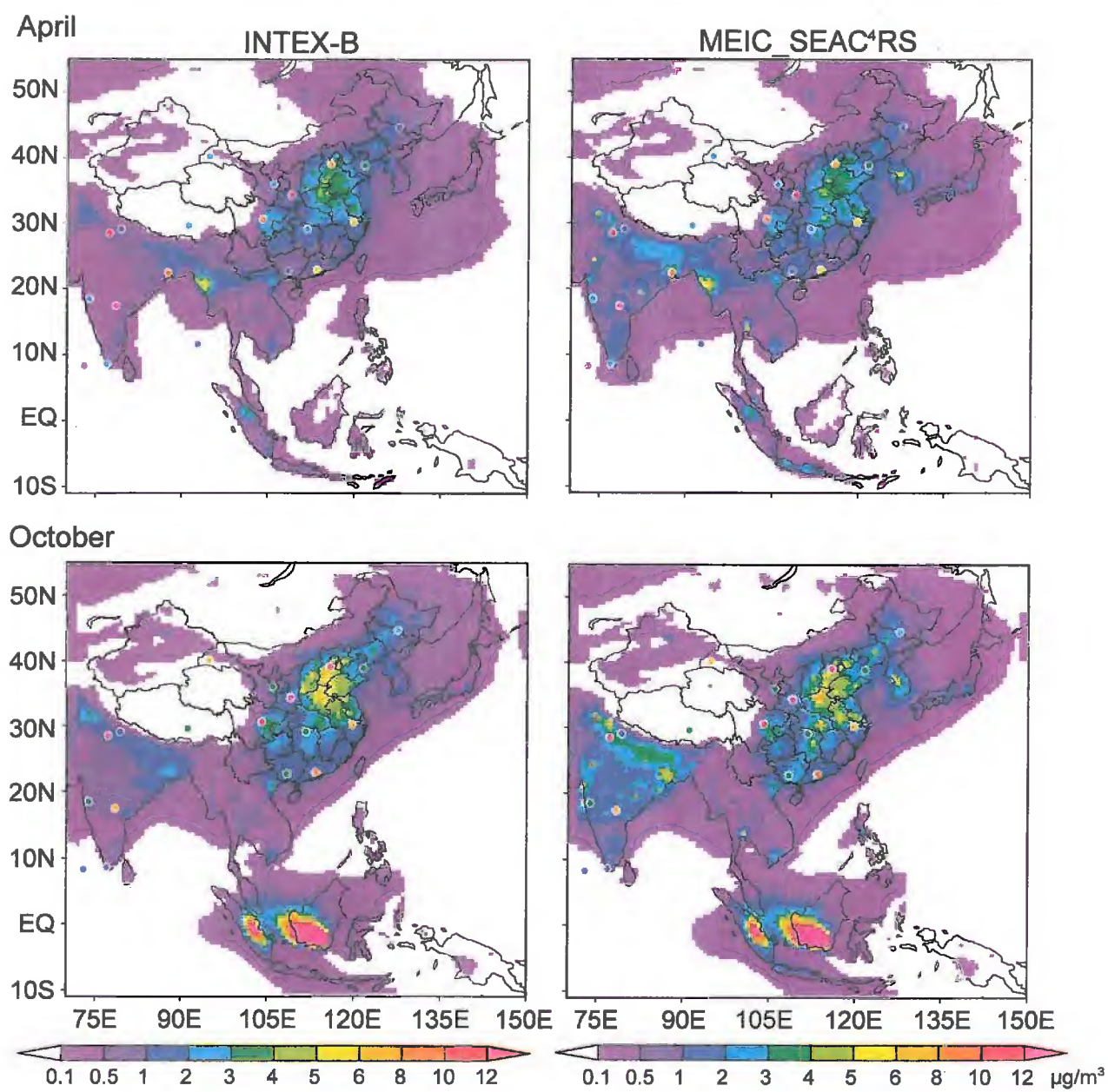
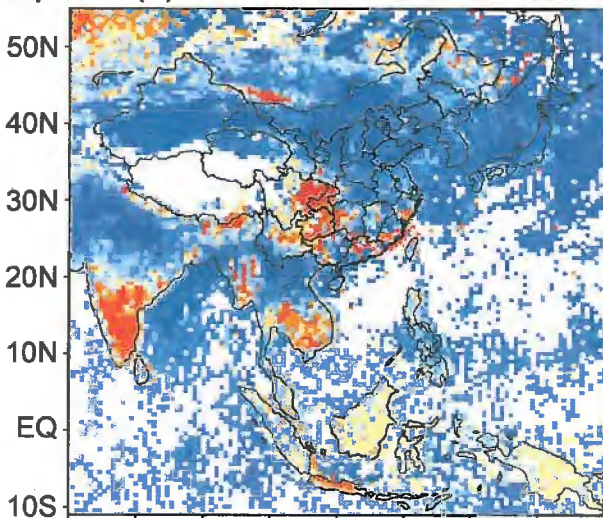


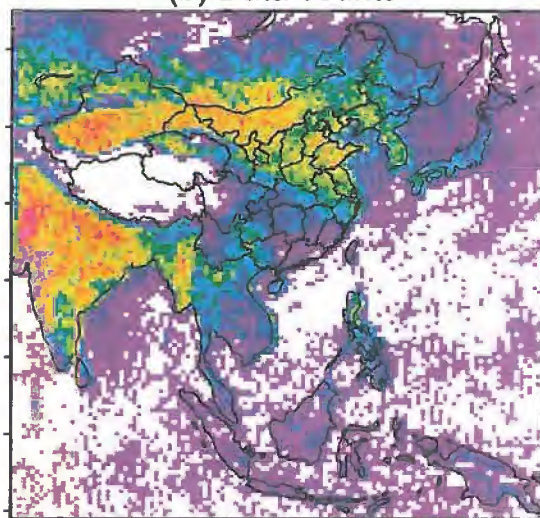
Fig. 5



April (a) GEOS-Chem minus OMI



(b) Data counts



October

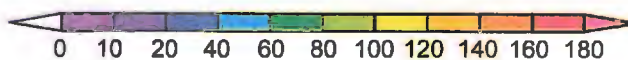
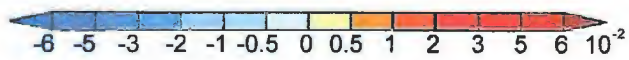
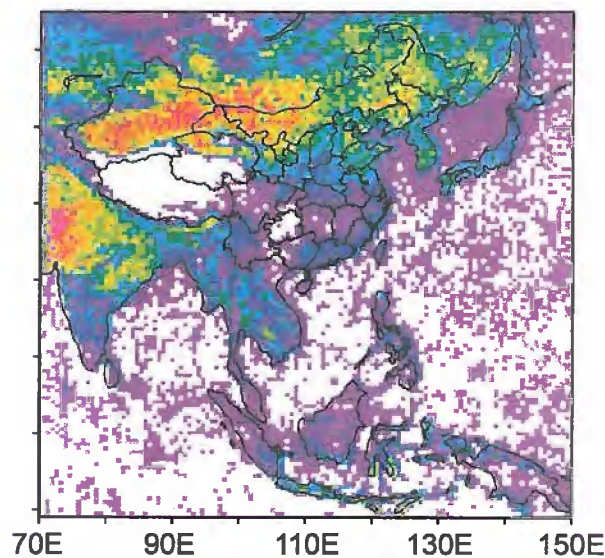
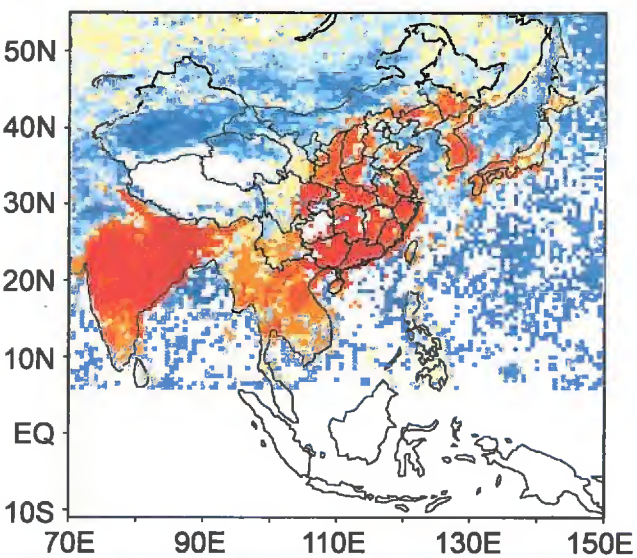


Fig. 6

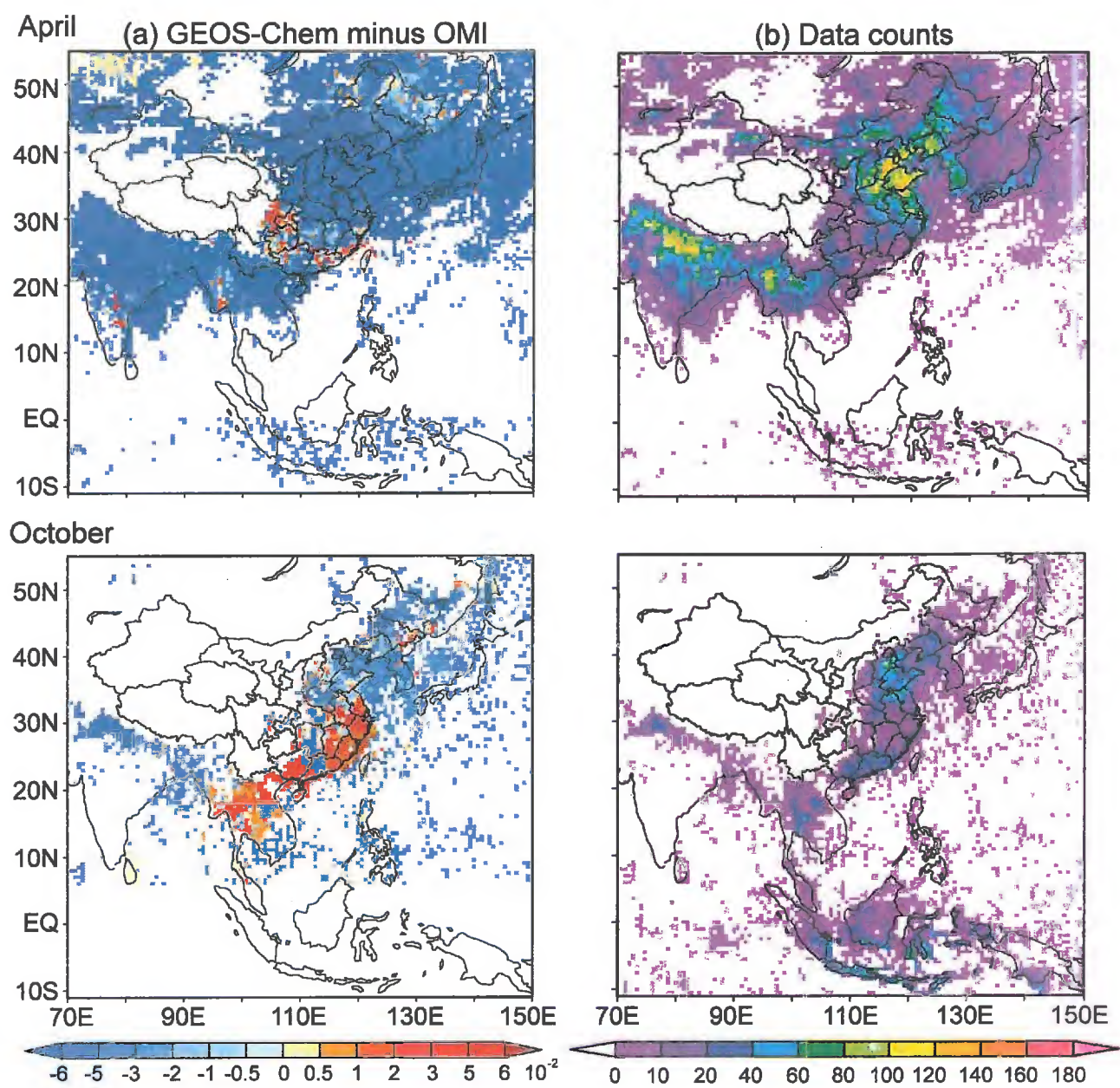


Fig. 7



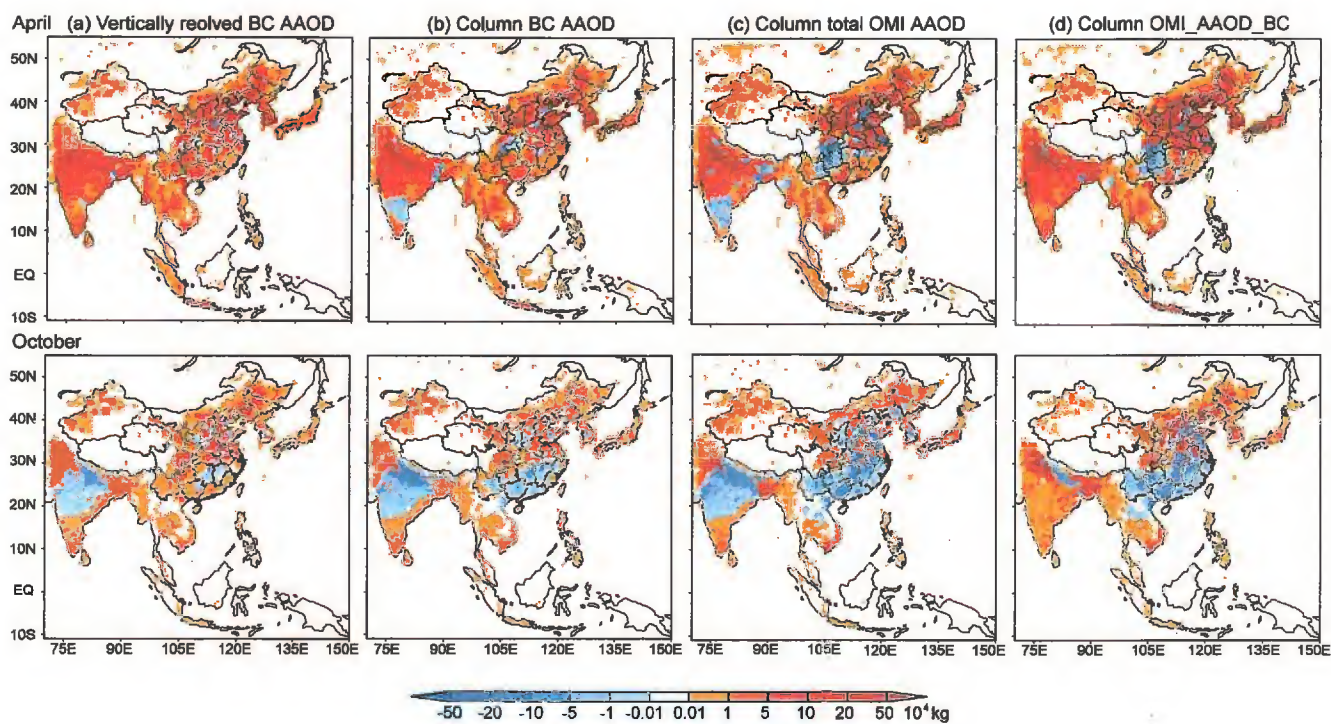


Fig. 8

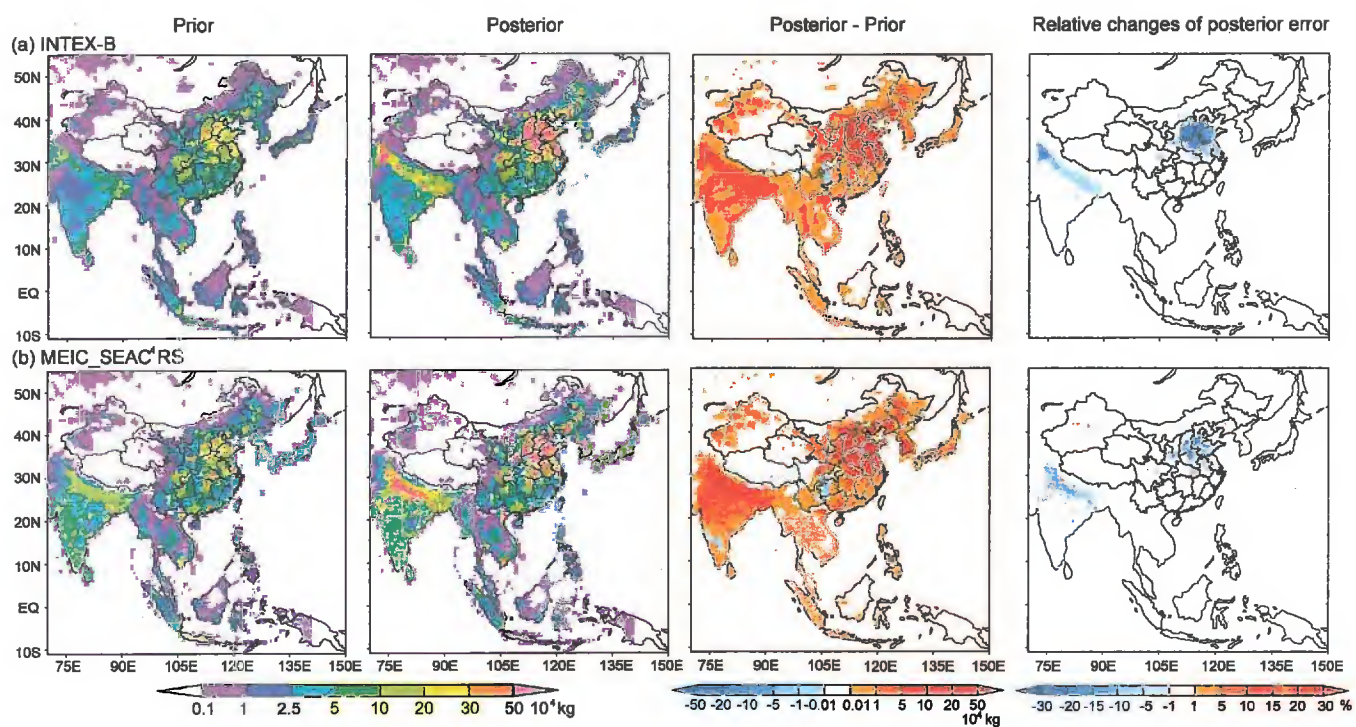


Fig. 9

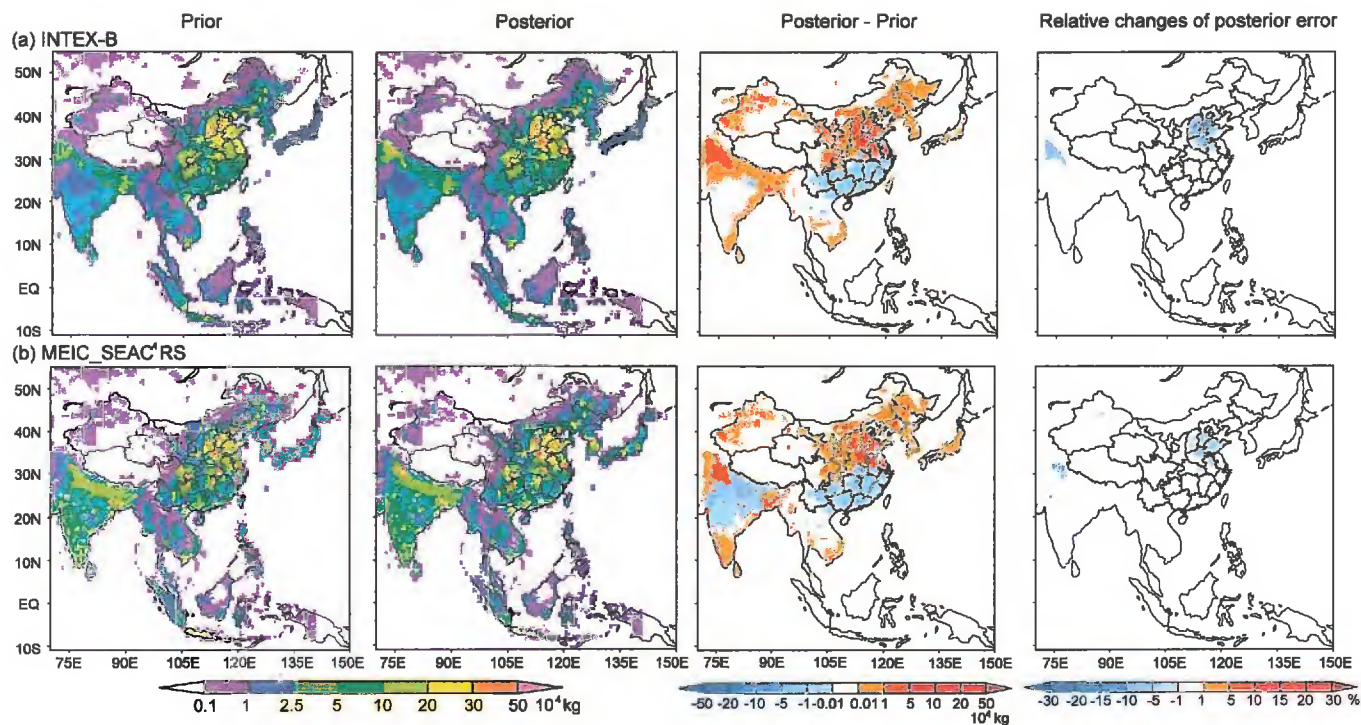


Fig. 10



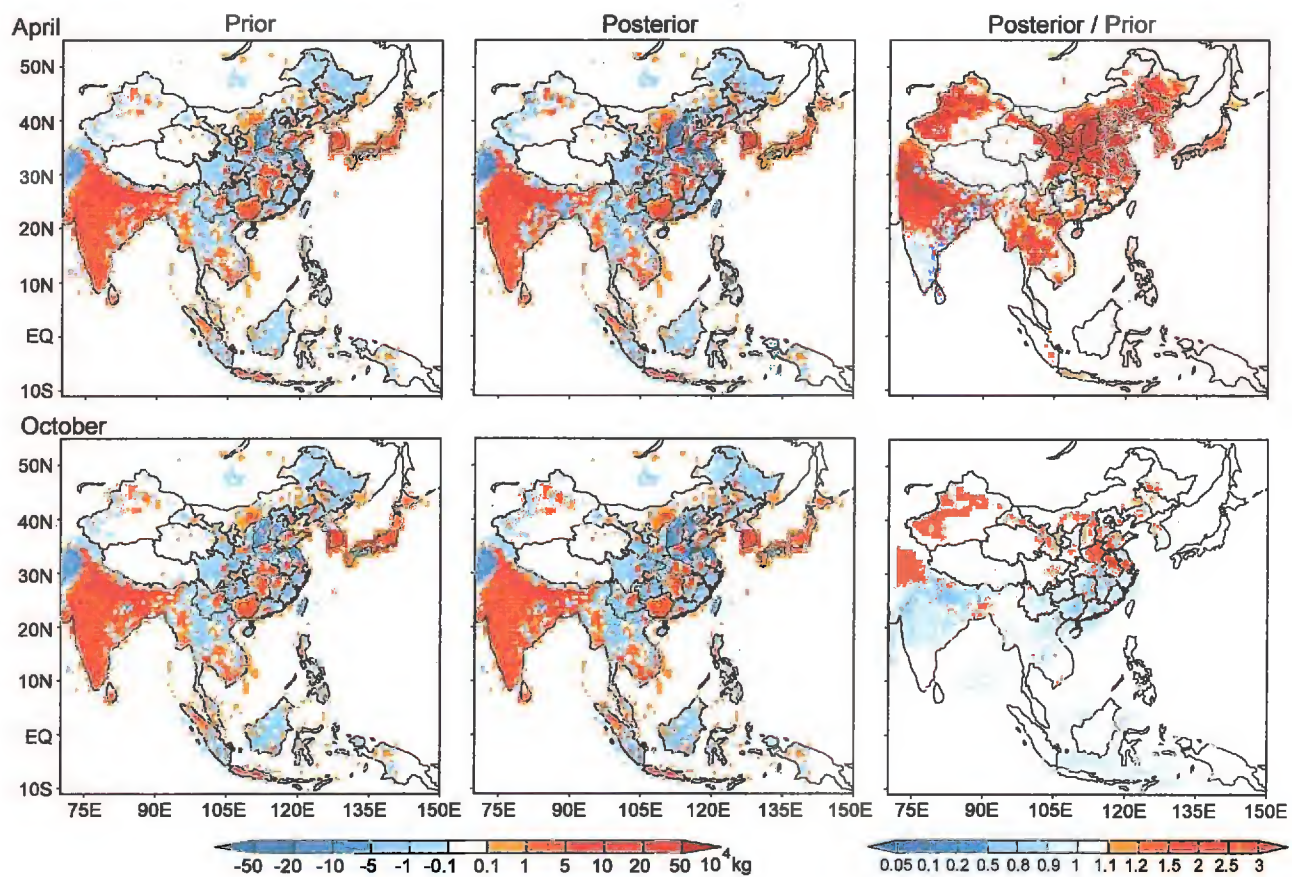


Fig. 11

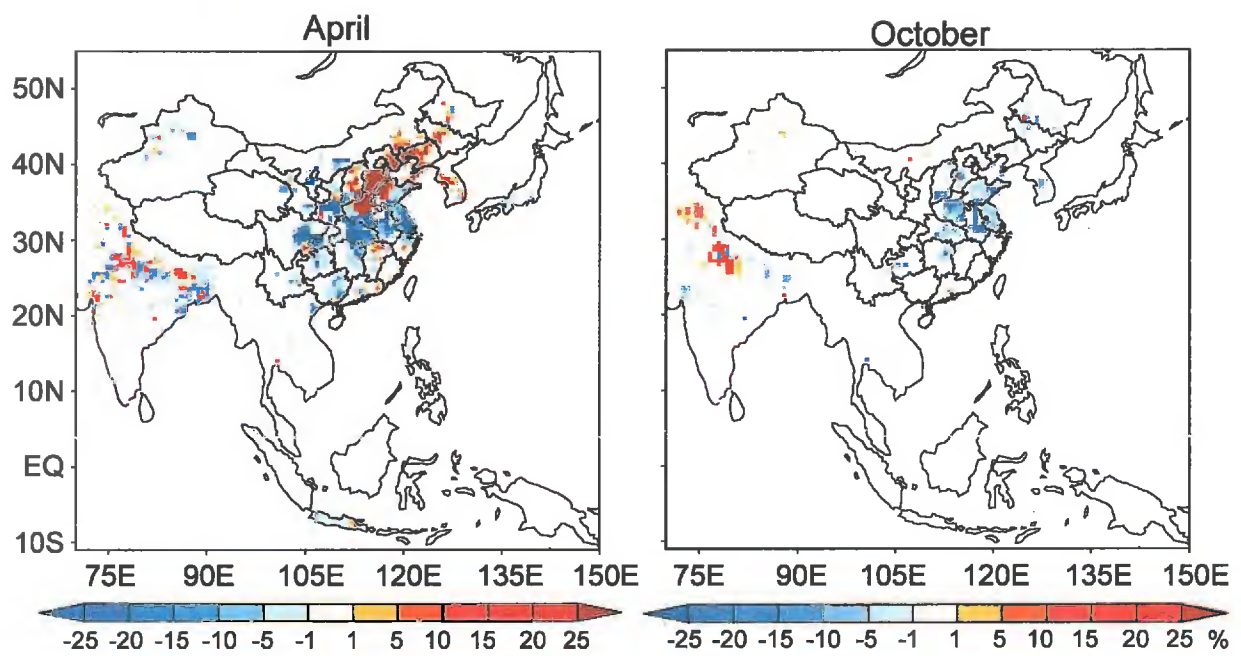
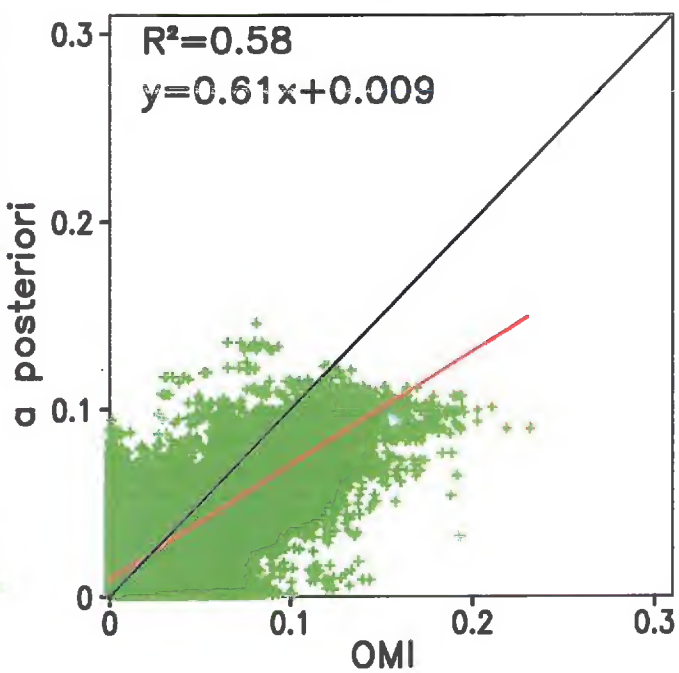
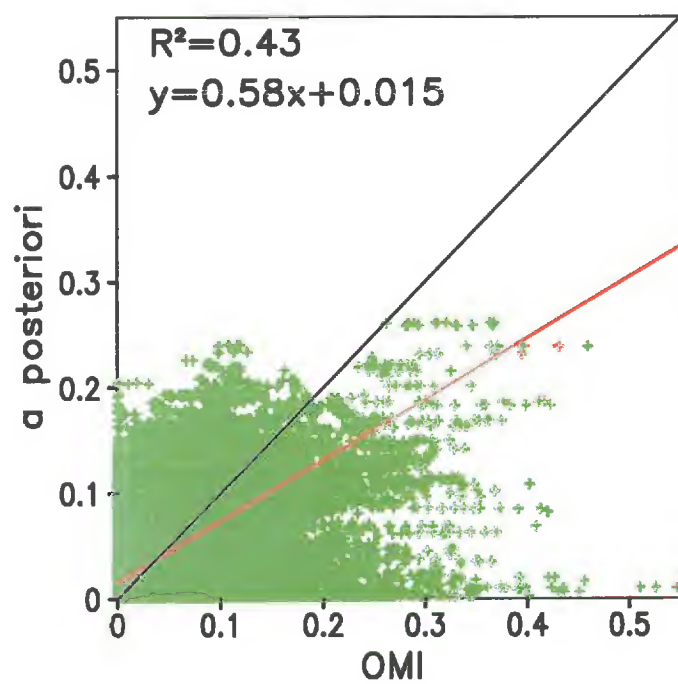
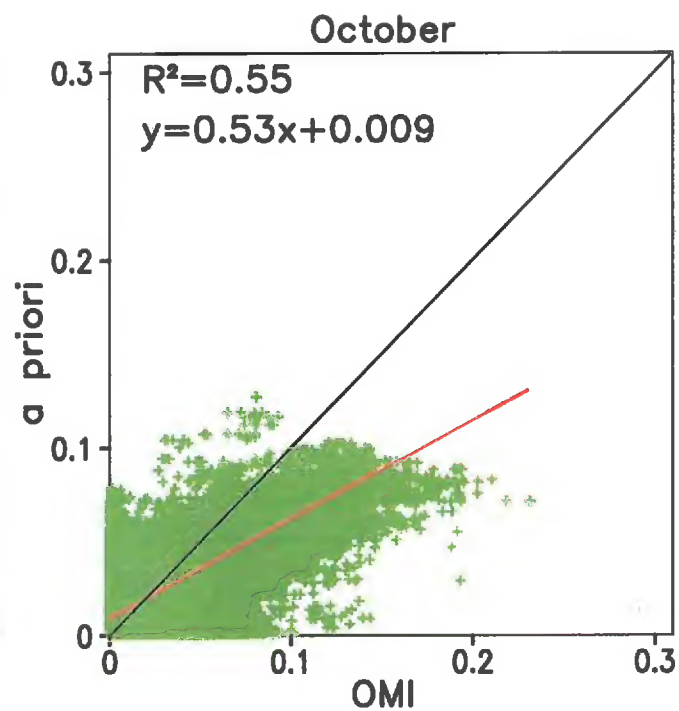
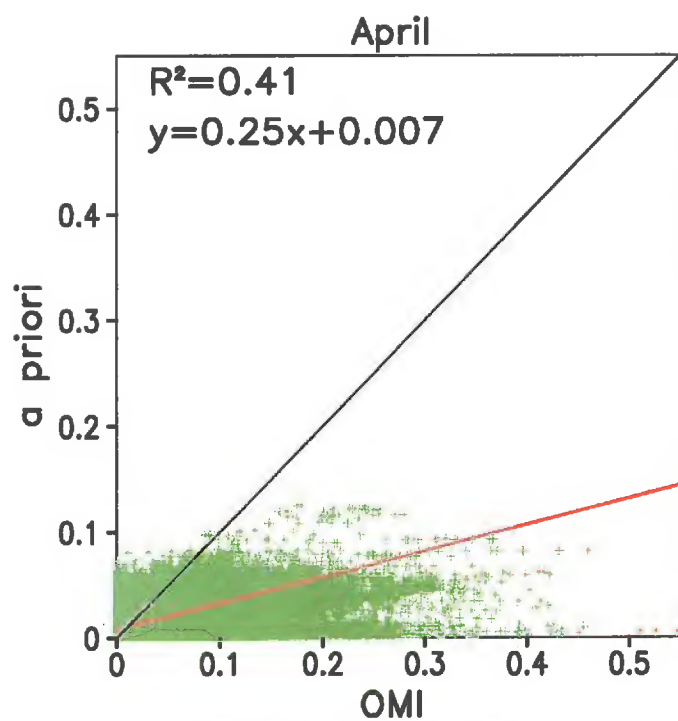
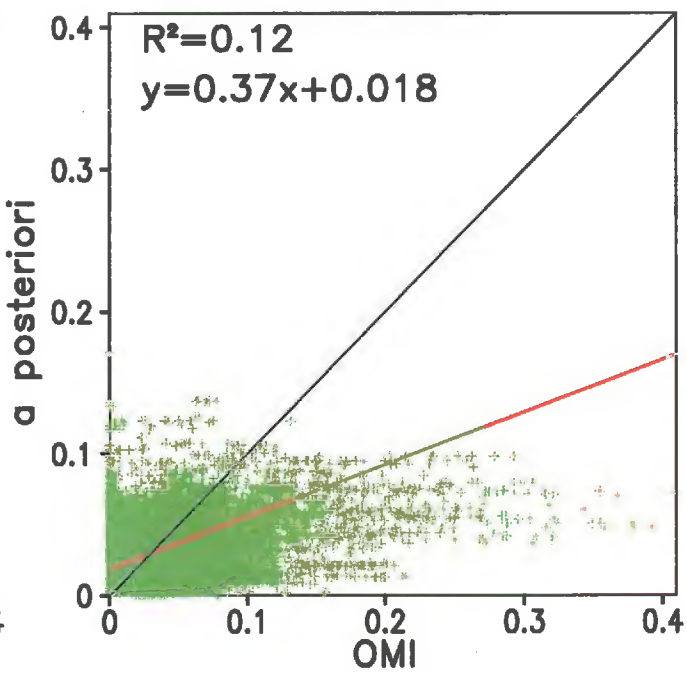
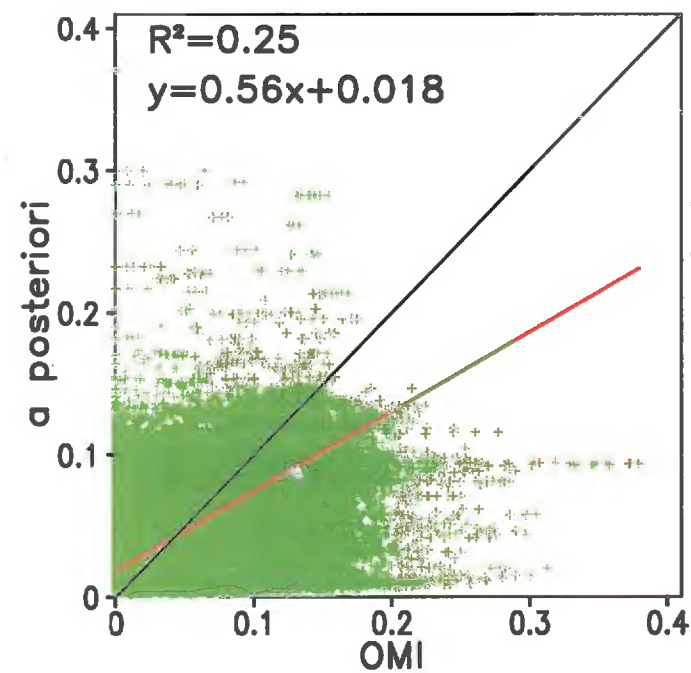
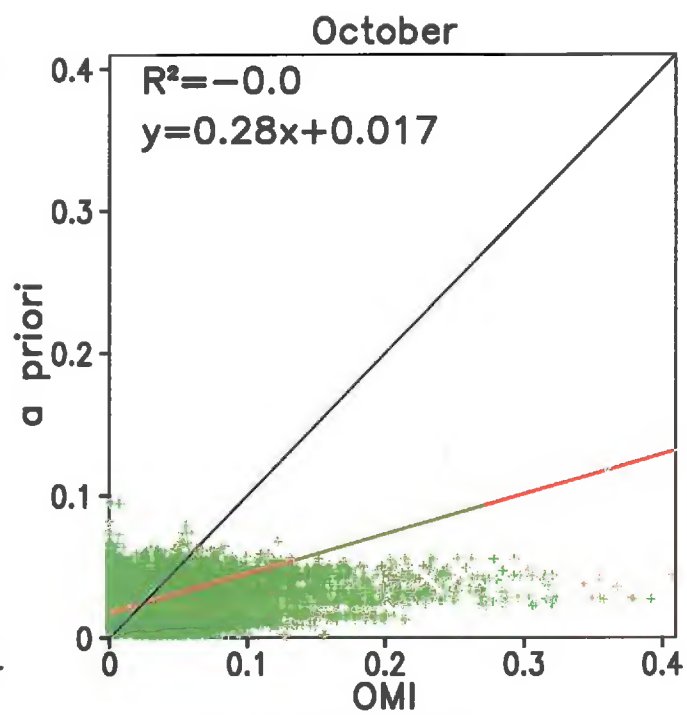
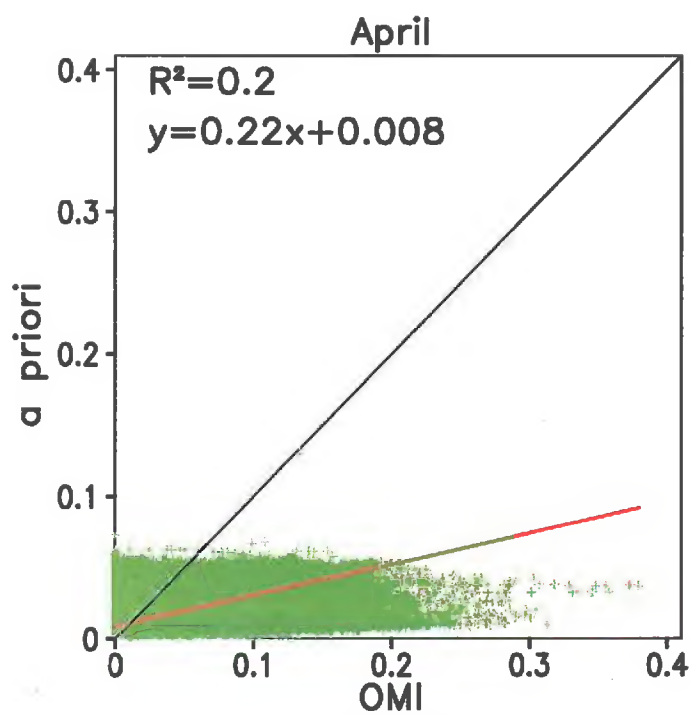


Fig. 12







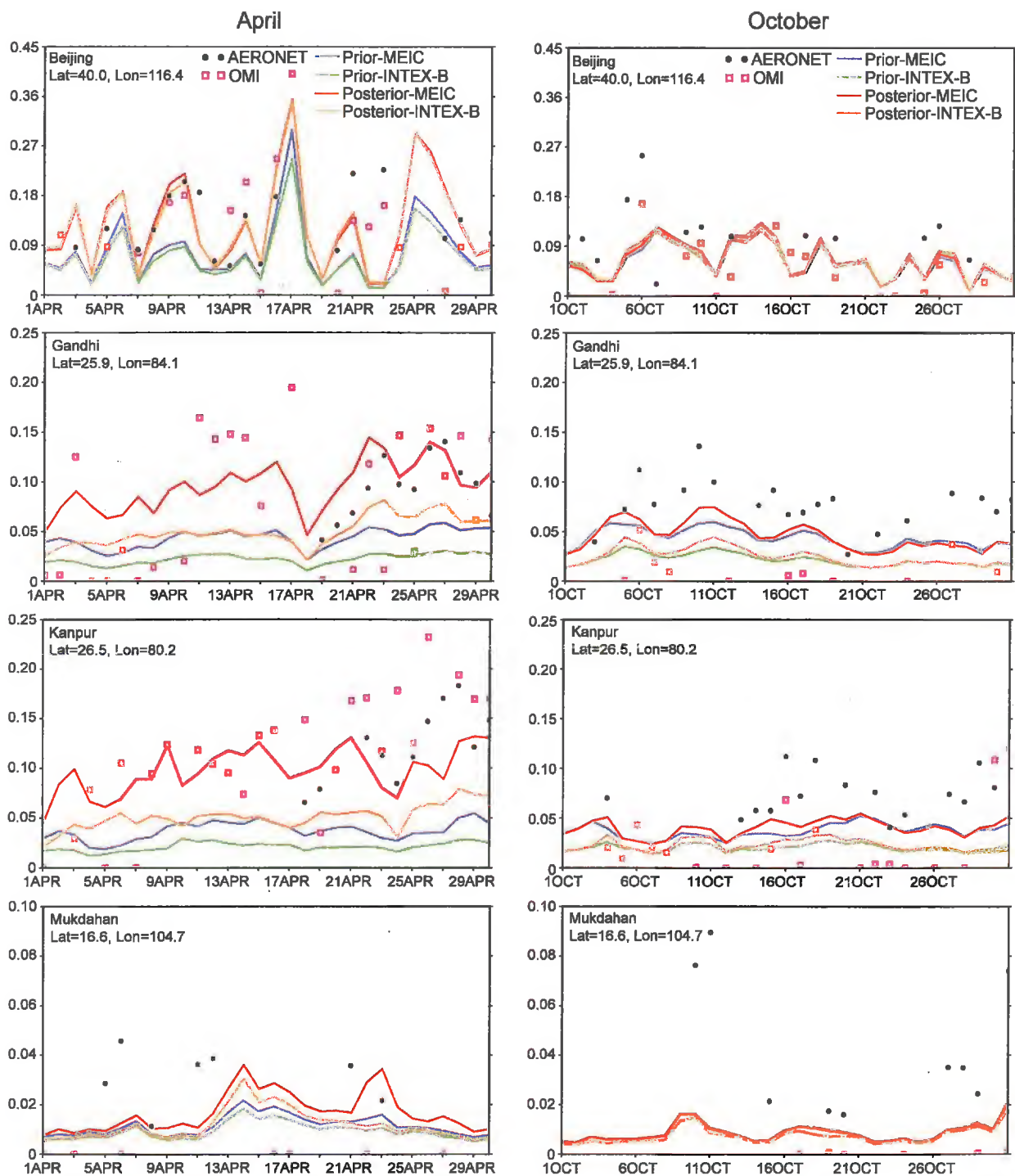


Fig. 15

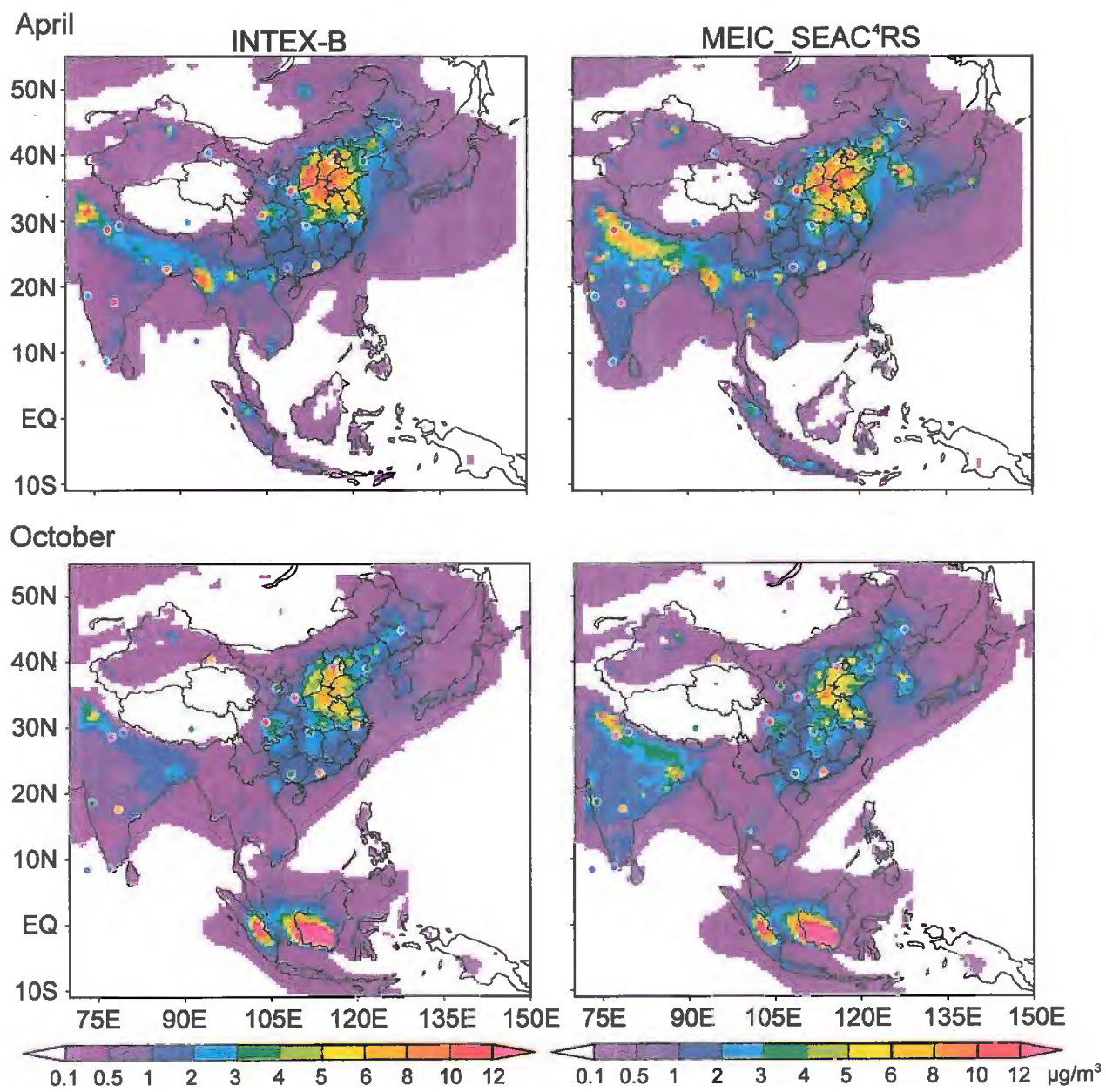


Fig. 16

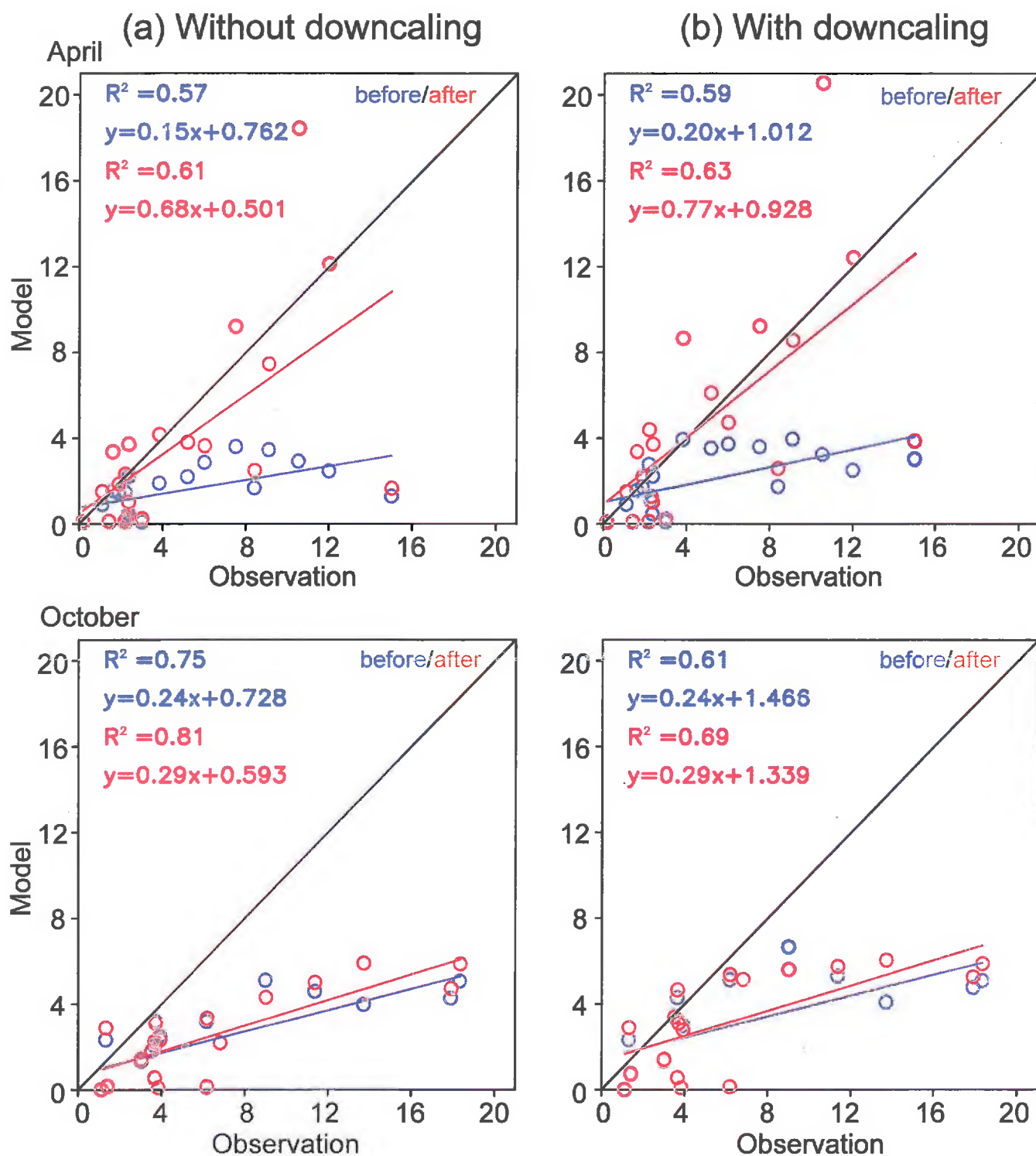


Fig. 17



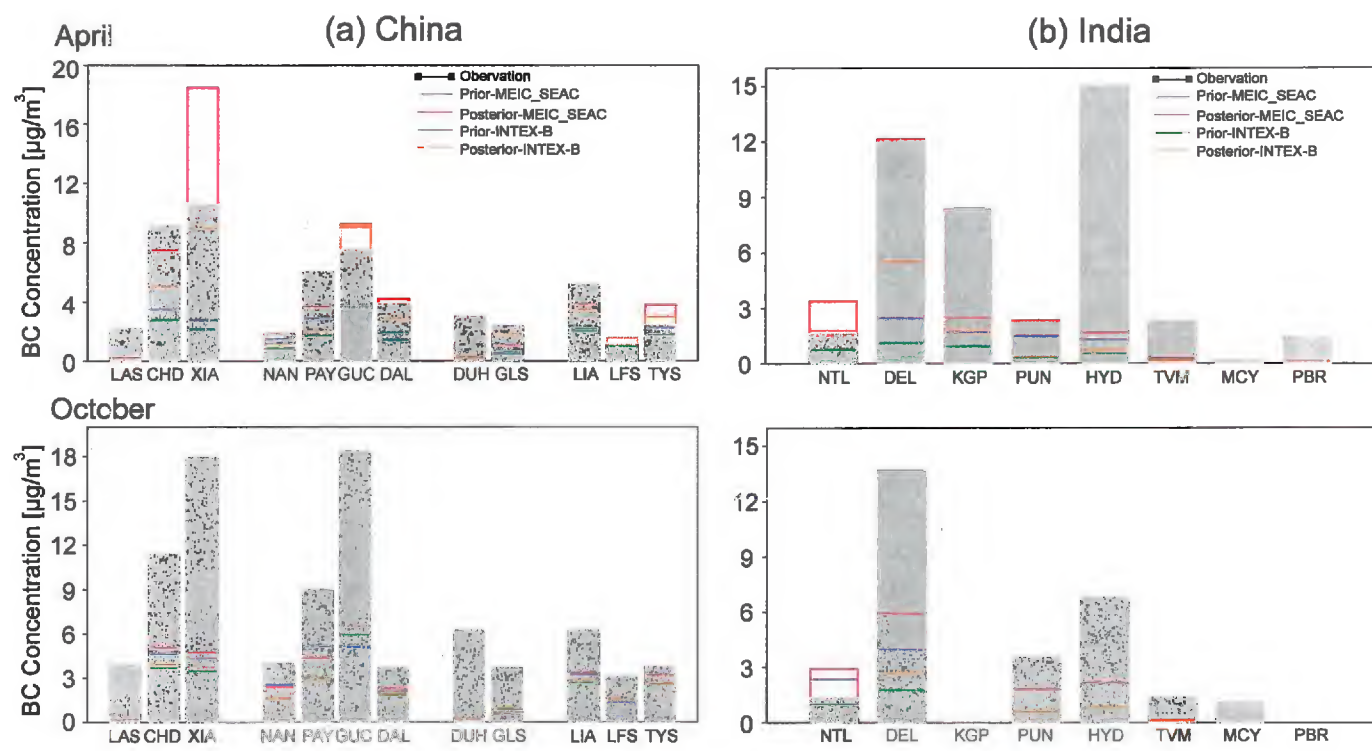


Fig. 18

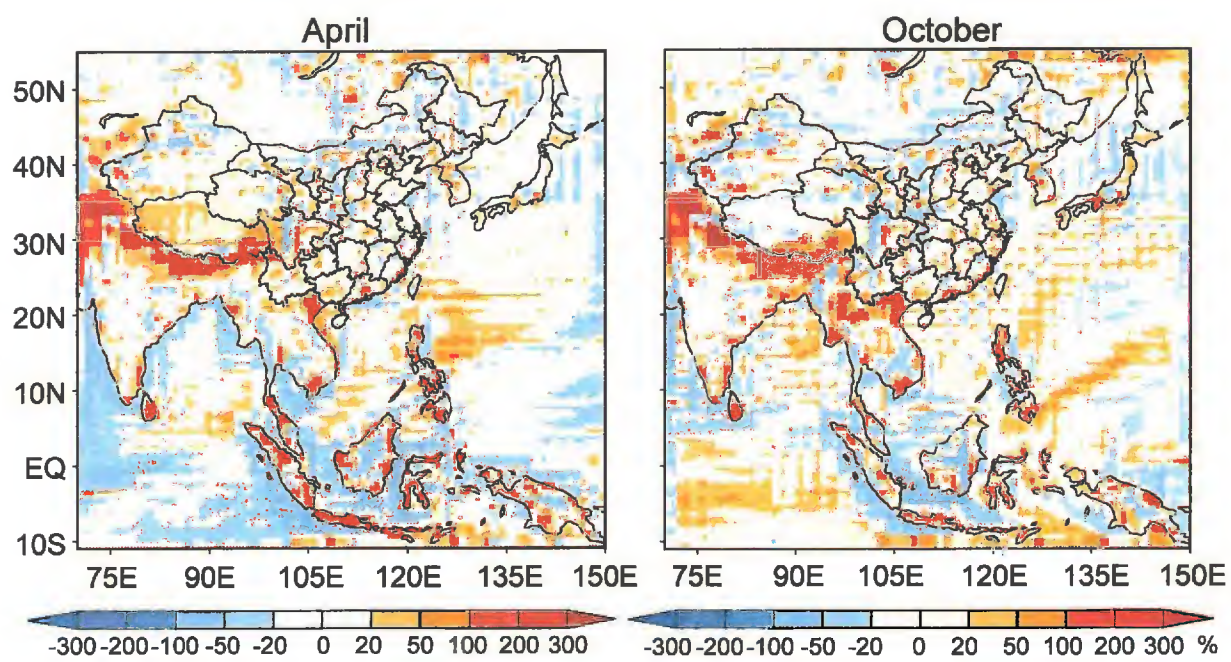


Fig. 19

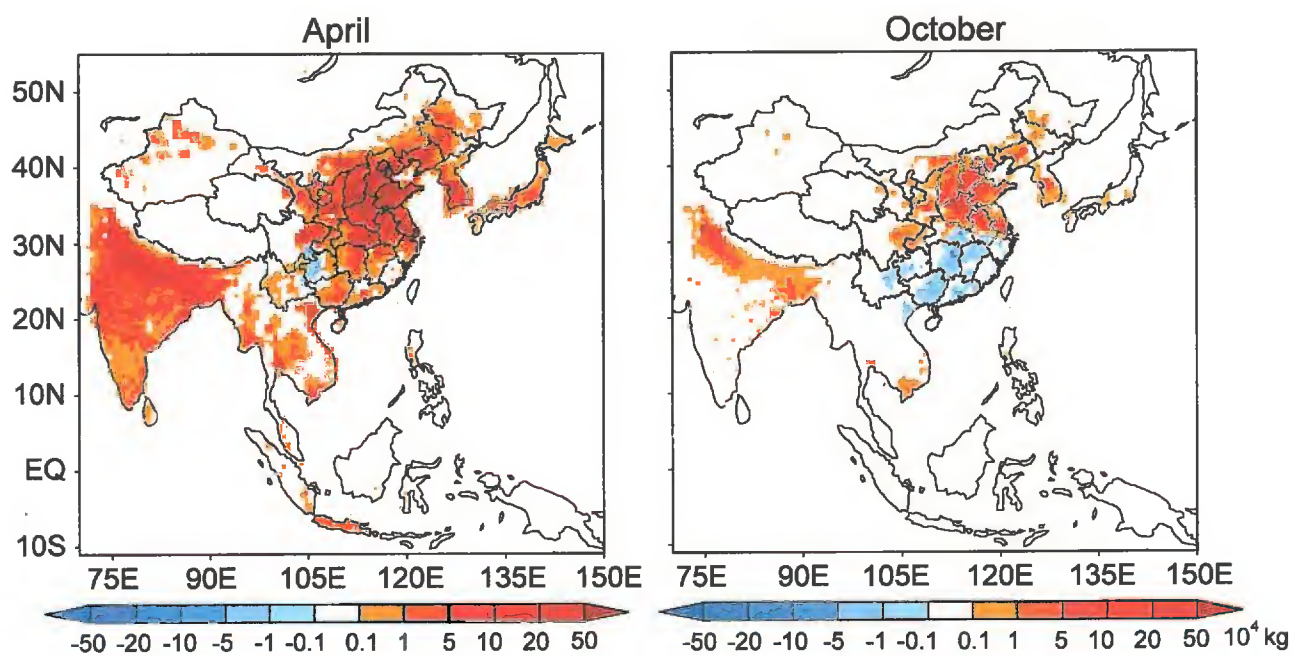


Fig. 20

